COMMUNICATIONS IN COMPUTATIONAL PHYSICS
Vol. **1**, No. 1, pp. 135-175

Commun. Comput. Phys.
February 2006

Variational Boundary Conditions for Molecular Dynamics Simulations of Solids at Low Temperature

Xiantao Li[1,*] and Weinan E[2]

[1] *Department of Mathematics, Pennsylvania State University, University Park, PA 16802, USA.*

[2] *Department of Mathematics & Program in Applied and Computational Mathematics, Princeton University, Princeton, NJ 08544, USA.*

Receive 25 September 2005; Accept (in revised version) 12 October 2005

Abstract. Boundary conditions for molecular dynamics simulation of crystalline solids are considered with the objective of eliminating the reflection of phonons. A variational formalism is presented to construct boundary conditions that minimize total phonon reflection. Local boundary conditions that involve a few neighbors of the boundary atoms and limited number of time steps are found using the variational formalism. Their effects are studied and compared with other boundary conditions such as truncated exact boundary conditions or by appending border atoms where artificial damping forces are applied. In general it is found that, with the same cost or complexity, the variational boundary conditions perform much better than the truncated exact boundary conditions or by appending border atoms with empirical damping profiles. Practical issues of implementation are discussed for real crystals. Application to brittle fracture dynamics is illustrated.

Key words: Boundary condition; molecular dynamics; phonon reflection; crack propagation.

1 Introduction

The main purpose of this paper is to present a systematic study of the boundary conditions for molecular dynamics (MD) simulation of crystalline solids at low temperature. We have in mind two kinds of problems: either the MD is done in isolation with some experimental loading conditions applied to the boundary of the MD domain, or it is coupled with a continuum model outside the MD region. It has been realized that in both cases, at low temperature, the key issue is to eliminate the reflection of phonons at the boundary of the MD region or the continuum-MD

*Correspondence to: Xiantao Li, Department of Mathematics, Pennsylvania State University, University Park, PA 16802, USA. Email: xli@math.psu.edu.

interface. Here we will present both the theoretical framework and the numerical procedure for constructing boundary conditions that accomplish this.

The problem, as formulated above, closely resembles the problem of absorbing boundary conditions for the numerical computation of wave propagation at the far field boundary where the computational domain is truncated [14,15]. Indeed our work is very much inspired by the work in that area. In the physical world, waves know of no boundaries as they propagate. But to compute them numerically, one has to truncate the domain somewhere in order to have a computational domain of finite size. At this artificially created boundary, some numerical boundary conditions have to be used for any kind of numerical algorithms. Ideally the numerical boundary conditions should be such that the computed solutions closely approximate the physical solutions in the infinite medium. Since there are no sources of waves outside the computational domain, this amounts to requiring that the waves are not reflected at the artificial boundary.

In principle, one can write down exact reflectionless boundary conditions. In section 2, we include a concise derivation of such exact boundary conditions. In practice, however, these exact boundary conditions are of little use since they are *nonlocal both in space and in time*. Furthermore, the influence kernels (also known as response functions, influence matrices, time history kernels etc) in these boundary conditions decay rather slowly. Therefore since the 70's, much effort has gone into finding approximate but *local* boundary conditions that eliminate wave reflection to high order accuracy. Most well-known among such boundary conditions are the absorbing boundary conditions proposed by Engquist and Majda [14, 15], which were based on approximating the Fourier symbols associated with the exact boundary conditions, by either Taylor expansion or Padé approximation in the regime of near normal incidence.

Our problem for MD is very similar in spirit. The main issue is again the formulation of boundary conditions so that phonons, the discrete lattice waves, are not reflected at the boundary. Indeed one can also write down exact boundary conditions that accomplish this. This was first done by Adelman and Doll for the simple one-dimensional discrete wave equation [1]. W. Cai et al. discussed how one can in principle obtain such exact boundary conditions in the general case via numerical computations. This amounts to computing the response functions for the boundary [6]. Karpov, Liu, Park, Wagner and co-workers continued with the path suggested by Adelman and Doll, and extended that formalism to general crystal structures [22, 27, 32].

Even though one can in principle obtain such exact boundary conditions, they have the same difficulty as for the wave equation: they are nonlocal in space and time, and the influence kernels decay rather slowly. Experience with the wave equations suggests that these exact boundary conditions may not be the most efficient tools for numerical computations. This is particularly an issue in coupled continuum-MD simulations where we expect the MD region to change as the computation proceeds. Therefore as for wave equations, it is of considerable practical interest to find approximate boundary conditions which are local. This idea was first pursued in the work of E and Huang [11, 12] for simplified models, and the present paper continues on that path.

At this point, it is important to note a crucial difference between the wave equation and MD: the wave equation is continuous and for that reason, as long as the waves are fully resolved by the numerical grid, we can use small wavenumber approximations. In contrast, MD is discrete and the phonon spectrum spreads over all wavenumbers. The boundary conditions that we devise

have to take into account phonons at all wavenumbers. Based on this consideration, [11, 12] proposed to design MD boundary conditions in such a way that some integrated quantities representing total phonon reflection are minimized. This idea was applied to some one and two dimensional examples, and the results were quite promising.

The present paper presents a systematic exploration of such variational boundary conditions for general lattices. First we formulate a variational principle for the minimization of total phonon reflection. Local boundary conditions are then derived based on this variational principle. These boundary conditions are compared with the exact boundary condition, and it is demonstrated that one can achieve almost the same effect as the exact boundary conditions, but at much less cost. As we increase the number of time steps involved in the local boundary conditions, we can recover the exact boundary condition in the limit of infinite number of time steps. Next we discuss various practical aspects of these local boundary conditions, including applications to complex crystal structure, three dimensional problems, efficient integration over the Brillouin zone, maintaining external loading etc. Finally we apply these boundary conditions to the simulation of crack propagation in solids.

A main issue that we are concerned with is the compactness of the boundary conditions. One idea that we explore is the use of a larger stencil in space (i.e. more atoms in space), and in turn we use much fewer number of time steps in the boundary conditions. To illustrate this point, we will derive alternative exact boundary conditions that involve more atoms. We show that by doing so, we achieve faster decay of the kernels in time.

A popular technique used by many people is to employ a border region where phonons are damped by adding damping terms to the equations of motion. While this technique is quite convenient to use, there does not seem to exist any theory for selecting the optimal profile for the damping coefficient, or assessing the effect of such a procedure. We will present an example to show that in the absence of such a theory, this technique may not be very reliable.

Since there is a close analogy between the issues addressed here and the absorbing boundary conditions for the wave equation, we begin in the next section by reviewing briefly the situation for wave equation. We then turn our attention to MD in section 3, discussing how the reflection matrix can be computed for a given boundary condition, and how local boundary conditions can be derived that minimize phonon reflection. In section 4 several implementation issues are discussed. Finally we test these local boundary condition in simulations of brittle fracture in section 5.

2 Boundary conditions for the wave equation

In order to understand the general formulation of the boundary conditions, we first discuss a continuous case: the wave equation. We assume that the sources of the waves, in the initial data, are contained in the right half space $x > 0$. Of course the waves will then propagate over the whole space. But we are only going to compute them in the right half space. For that purpose, we will have to impose artificial boundary conditions at $x = 0$. Ideally the boundary condition has to be such that the computed solution coincides with the exact solution when the

wave equation is solved over the whole space.

2.1 Exact boundary condition

There does exist boundary conditions that fulfill the requirement stated above. These are called exact boundary conditions. To derive the exact boundary condition, we solve the wave equation in the left half-space,

$$\begin{aligned} u_{tt} &= c^2\Delta u, \quad x<0, \\ u(x,y,0) &= 0, \\ u_t(x,y,0) &= 0, \\ u(0,y,t) &= u_0(y,t). \end{aligned} \tag{2.1}$$

Taking the Fourier transform in y and Laplace transform in t, and letting

$$\hat{u}(x,k,s) = \mathcal{F}_{y\to k}\mathcal{L}_{t\to s}[u].$$

we then have,

$$\hat{u}_{xx} = (s^2/c^2 + k^2)\hat{u},$$

and so

$$\hat{u}(x,k,s) = e^{x\sqrt{(s/c)^2+k^2}}\widehat{u_0}(k,s).$$

This implies that for any $x<0$,

$$u(x,y,t) = \int_0^t \int_{\mathbb{R}} G(x,y-\eta,t-\tau)u_0(\eta,\tau)d\eta d\tau, \tag{2.2}$$

where,

$$\mathcal{F}_{y\to k}\mathcal{L}_{t\to s}[G] = e^{x\sqrt{(s/c)^2+k^2}}.$$

The kernel $G(x,y,t)$ is computed numerically and plotted in Fig. 1 for $c\equiv 1$, and $x=-1$. Similar boundary conditions have been derived for discrete wave equations [3, 13, 18].

2.2 Absorbing boundary condition

The exact boundary condition (2.2) is non-local in both space and time, which makes it impractical for numerical implementations. Therefore effort has been made to derive approximations of (2.2) that are local in character. One class of local boundary conditions, known as absorbing boundary condition (ABC), has been developed in [14, 15]. ABC aims at absorbing waves that move toward the boundary so that they are not reflected. To derive such boundary condition, one first considers left-moving wave packets expressed as a Fourier integral,

$$u(x,y,t) = \int\int e^{i(\sqrt{\omega^2-\xi^2}\,x+\xi y+\omega t)}\widehat{u_0}(\xi,\omega)d\xi d\omega. \tag{2.3}$$

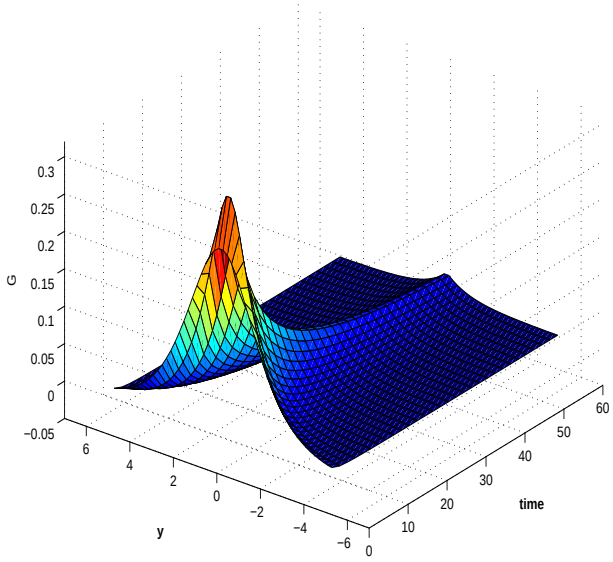

Figure 1: The kernel $G(x,y,t)$ in the exact boundary condition (2.2).

In this case one can easily find the exact boundary condition,

$$\begin{aligned}\frac{\partial}{\partial x}u(0,y,t) &= \int\int e^{i(\xi y+\omega t)} i\sqrt{\omega^2-\xi^2}\,\widehat{u_0}(\xi,\omega)d\xi d\omega \\ &= \sqrt{\frac{\partial^2}{\partial t^2}-\frac{\partial^2}{\partial y^2}}\,u_0(y,t),\end{aligned} \tag{2.4}$$

through a non-local operator.

The next step is to approximate the operator by a local one. For ξ/ω small, namely near normal incidence, one can approximate,

$$i\sqrt{\omega^2-\xi^2} = i\omega\sqrt{1-(\xi/\omega)^2},$$

by a Taylor or Padé expansion. For instance, the first order approximation yields,

$$i\sqrt{\omega^2-\xi^2} = i\omega\big(1+O(\xi^2/\omega^2)\big),$$

which corresponds to the first order time derivative, and gives

$$\Big(\frac{\partial}{\partial x}-\frac{\partial}{\partial t}\Big)u\Big|_{x=0} = 0.$$

The next order expansion,

$$i\sqrt{\omega^2-\xi^2} = i\omega\big(1-\frac{1}{2}\xi^2/\omega^2+O(\xi^4/\omega^4)\big),$$

leads to,

$$\Big(\frac{\partial^2}{\partial t\partial x}-\frac{\partial^2}{\partial t^2}+\frac{1}{2}\frac{\partial^2}{\partial y^2}\Big)u\mid_{x=0}=0.$$

Following the same procedure, a hierarchy of boundary conditions are derived in [14, 15].

Given a boundary condition defined through an operator $B(\xi,\omega)$, namely

$$\frac{\partial}{\partial x}u(0,y,t)=\int\int B(\xi,\omega)\hat{u}_0(\xi,\omega)e^{i(\xi y+\omega t)}d\xi d\omega, \tag{2.5}$$

one can calculate the amount of wave reflection due to the applied boundary condition. To see this, we consider solutions of the form:

$$u(x,y,t)=e^{i(\sqrt{\omega^2-\xi^2}\,x+\xi y+\omega t)}+R(\xi,\omega)e^{i(-\sqrt{\omega^2-\xi^2}\,x+\xi y+\omega t)}. \tag{2.6}$$

Substituting (2.6) into (2.5), we get

$$R(\xi,\omega)=-\frac{B-i\sqrt{\omega^2-\xi^2}}{B+i\sqrt{\omega^2-\xi^2}}. \tag{2.7}$$

3 Boundary conditions for molecular dynamics

Now we turn to boundary conditions for molecular dynamics (MD). In MD, the system is described by the position and momentum of each individual atom in the system. The dynamics of the atoms obey Newton's law:

$$m_i\ddot{\mathbf{R}}_i=-\nabla_{\mathbf{R}_i}V, \tag{3.1}$$

where m_i denotes the mass of the ith atom, and $V(\mathbf{R}_1,\mathbf{R}_2,\cdots,\mathbf{R}_N)$ is the interatomic potential.

We will set up the problem in the same way as we did for the continuous case. Let $\mathbf{n}$ be the inward normal vector of the boundary, pointing into the computational domain. A two dimensional example is shown in Fig. 2 for triangular lattice with $\mathbf{n}=(1,0)$. We will assume that the boundary coincides with a plane of major symmetry, including mirror symmetry. Without loss of generality, we designate the atom with index 0 as a boundary atom, and $\mathbf{r}_0=0$. We will assume that the lattice has a basis consisting of basis vectors $\{\mathbf{t}_i, i=1,2,\cdots,d\}$ with d being the dimension. The corresponding basis in the wavenumber space is $\{\mathbf{k}_j, j=1,2,\cdots,d\}$ with standard normalization [4],

$$\mathbf{t}_i\cdot\mathbf{k}_j=2\pi\delta_{ij}.$$

Throughout the paper, we will use $\hat{f}$ to represent the Fourier transform of f and $\tilde{f}$ for the Laplace transform of f.

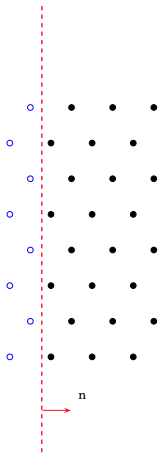

Figure 2: Boundary condition for molecular dynamics on a triangular lattice: the filled circles indicate atoms inside the computational domain; the open circles represent boundary atoms, the displacement of which is needed in the force calculation of the inside atoms. In the case when only nearest neighbor interaction is present, boundary conditions are needed for the two layers of boundary atoms next to the boundary, as shown in the picture.

3.1 Exact boundary condition

In the case when the atomic interaction is linear, it is possible to find the exact boundary condition, which expresses the displacement of the boundary atom in terms of the trajectory of the atoms inside of the computational domain. In [1,2,18] it was found that for one dimensional models, the boundary condition takes the form

$$u_0(t) = \sum_{j\geq 1} \int_0^t \beta_j(t-\tau) u_j(\tau) d\tau. \tag{3.2}$$

The time history kernel $\beta_j(t)$ describes the response of the boundary atom to the displacement of the jth atoms.

We now show for multi-dimensional lattices, the exact boundary condition can also be found. The procedure, which will be illustrated for the 3D case, $d = 3$, is very similar to that presented in the previous section. We first switch the indices of an atom from i to a triple index (i, j, k) which label the components in the selected basis vectors of the lattice. Without loss of generality, we assume that the normal vector coincides with the basis vector $\mathbf{t}_1$. In the case when the interatomic force is linear, the equation of motion can be written as,

$$M\ddot{\mathbf{u}}_{i,j,k} = -\sum_{l,m,n} D_{i-l,j-m,k-n}\mathbf{u}_{l,m,n}, \tag{3.3}$$

with u being the displacement and M being the mass matrix. One can reduce the summation over the first index to $-N_e \leq l \leq N_e$ for some integer N_e which represents the effective range of

the interatomic potential. To set up such equations for a complex lattice with n_a atoms in each primitive cell, the atoms in each cell are grouped together and an extended displacement vector is defined. The length of the extended vector is $S = 3n_a$. For simple lattice, S is equal to the dimension.

Taking Fourier transform in the $\mathbf{t}_2$ and $\mathbf{t}_3$ directions, we arrive at,

$$M\ddot{\mathbf{U}}_i(\eta,\zeta,t) = \sum_l \hat{D}_{i-l}(\eta,\zeta)\mathbf{U}_l(\eta,\zeta), \tag{3.4}$$

where

$$\mathbf{U} = \mathcal{F}_{j\to\eta,k\to\zeta}[\mathbf{u}], \hat{D} = \mathcal{F}_{j\to\eta,k\to\zeta}[D],$$

are the Fourier transform of the displacement and the force constant respectively.

Since we are only interested in what happens in the computational domain, e.g. $i > N_e$, we may assume that

$$\mathbf{u}_{i,j,k}(0) = \dot{\mathbf{u}}_{i,j,k}(0) = 0, \text{ for } i \le N_e.$$

Namely outside of the computational domain, the system is at zero temperature.

By taking the Laplace transform in time, and letting

$$\tilde{\mathbf{U}}(\eta,\zeta,s) = \mathcal{L}_{t\to s}\mathbf{U}(\eta,\zeta,t).$$

we get the following difference equations,

$$s^2 M\tilde{\mathbf{U}}_i = \sum_l \hat{D}_{i-l}\tilde{\mathbf{U}}_l, i \le N_e. \tag{3.5}$$

In order to find the general solution of the difference equation, we follow the standard procedure and seek solutions with the form of,

$$\tilde{\mathbf{U}}_i = \lambda^i \boldsymbol{\varepsilon}.$$

This leads us to considering the algebraic equation,

$$\det\Big|\sum_{l=-N_e}^{N_e} \hat{D}_l\lambda^l + s^2 MI\Big| = 0. \tag{3.6}$$

Assuming that $\det\hat{D}_{Ne} \neq 0$, we get a polynomial with degree $2 \times S \times N_e$.

Consider first the case when $|\lambda| = 1$, and let $\lambda = e^{i\xi}$. The above equation (3.6) implies that the matrix

$$\mathcal{D}(\xi) = \sum_l \hat{D}_l e^{il\xi},$$

has a negative eigenvalue. This matrix, which will be defined later, is known as the dynamic matrix. In order for the crystal to be stable, this matrix has to be positive definite. Hence this case is ruled out.

Because of the mirror symmetry of the crystal with respect to the boundary, we have

$$\hat{D}_l = \hat{D}^*_{-l}.$$

The symbol * here indicates the conjugate transpose. This shows that if λ is a solution, then the conjugate reciprocal, $1/\bar{\lambda}$, is also a solution. Therefore the number of solutions with $|\lambda| < 1$ is exactly SN_e. These modes shall be excluded to avoid exponential growth toward $-\infty$. We choose the modes

$$\{\lambda_l, |\lambda_l| > 1, l = 1, 2, \cdots, SN_e\},$$

with the corresponding linearly independent eigenvectors,

$$\{\boldsymbol{\varepsilon}_l, l = 1, 2, \cdots, SN_e\}.$$

The general solution to the difference equation can now be written as,

$$\tilde{\mathbf{U}}_i = \sum_l c_l \lambda_l^i \boldsymbol{\varepsilon}_l. \tag{3.7}$$

with the constants c_l. In particular, for the boundary atom,

$$\tilde{\mathbf{U}}_0 = \sum_l c_l \boldsymbol{\varepsilon}_l.$$

It remains to find the coefficients c_l. Given $\tilde{\mathbf{U}}_l, l = 1, 2, \cdots, N_e$, substitutions can be made to (3.7), which leads to a linear system for these coefficients. As a result, $\tilde{\mathbf{U}}_0$ is expressed in terms of these prescribed values,

$$\tilde{\mathbf{U}}_0 = \sum_l \Theta_l \tilde{\mathbf{U}}_l, \tag{3.8}$$

where Θ_l's are some S-by-S matrices.

Now applying an inverse Laplace transform in s and inverse Fourier transform in (η, ζ), and we obtain the exact boundary condition in the following form,

$$\mathbf{u}_{0,j,k}(t) = \sum_m \sum_n \int_0^t \boldsymbol{\theta}_{l,j-m,k-n}(t-\tau)\mathbf{u}_{l,m,n}(\tau)d\tau, \tag{3.9}$$

where,

$$\mathcal{L}_{t\to s}\mathcal{F}_{m\to\eta,n\to\zeta}[\theta_{l,m,n}] = \Theta_l(\eta, \zeta, s).$$

This procedure is quite general. Another systematic procedure has been developed in [22, 32] to derive the kernels $\boldsymbol{\theta}$. From (3.7) it is possible to represent any other atom outside of the computational domain using different time history kernels. It is also noteworthy that in multi-dimension the exact boundary condition is nonlocal in both time and space; it requires that the displacement of the atoms on the next N_e layers be given for all previous time.

As an example, we consider a 1D chain of atoms connected by springs. After linearizing the Newton's equation at the equilibrium configuration, one gets the equation,

$$m\ddot{u}_j = K\big(u_{j+1} - 2u_j + u_{j-1}\big)/a^2. \tag{3.10}$$

for the displacement. Using $\{K, m, a\}$ as unit for energy, mass and length, we nondimensionalize the equation (3.10) to,

$$\ddot{u}_j = u_{j+1} - 2u_j + u_{j-1}.$$

With the help of Laplace transform, the following difference equation,

$$s^2\tilde{u}_j = \tilde{u}_{j+1} - 2\tilde{u}_j + \tilde{u}_{j-1},$$

is obtained, with two modes given by,

$$\lambda_\pm = 1 + \frac{s^2}{2} \pm \frac{s}{2}\sqrt{s^2+4}.$$

By choosing λ_+, we have

$$\tilde{u}_j = C\lambda_+^j, \tag{3.11}$$

for some C depending only on s. In particular,

$$\tilde{u}_1 = \lambda_+\tilde{u}_0.$$

Therefore,

$$\Theta(s) = \lambda_+ = 1 + \frac{s^2}{2} - \frac{s}{2}\sqrt{s^2+4}.$$

An inverse Laplace transform yields,

$$\theta(t) = \frac{2J_2(2t)}{t}, \tag{3.12}$$

and

$$u_0(t) = \int_0^t \theta(\tau)u_1(t-\tau)d\tau.$$

The function J_2 is the Bessel function of the first kind. For large t these Bessel functions have the following asymptotic approximation,

$$J_n(t) \sim \sqrt{\frac{2}{\pi t}}\cos(t - \frac{n}{2} - \frac{\pi}{4}).$$

Hence the kernel decays like $t^{-3/2}$ as t approaches to infinity.

Exact boundary conditions are not unique. For instance one may choose the following form of the exact boundary condition,

$$u_0(t) = \int_0^t \theta_j(\tau)u_j(t-\tau)d\tau, \tag{3.13}$$

for any $j > 1$. Since $\tilde{u}_0 = \tilde{\theta}\tilde{u}_1 = \tilde{\theta}^2\tilde{u}_2 = \cdots$ from (3.11), we have,

$$\widetilde{\theta_j} = \tilde{\theta}^j.$$

The kernel $\theta_j(t)$, which reflects the influence of the jth atom on the boundary atom, has the same decay rate as $\theta(t)$. However, if we include more atoms and consider boundary conditions of a more general form:

$$u_0(t) = \sum_{j=1}^{J} \int_0^t \alpha_j(\tau) u_j(t-\tau) d\tau, \tag{3.14}$$

we may be able to obtain history kernels that have faster decay rates. Next we will explain how this can be done.

We begin the derivation by extending the functions $\alpha_j(t)$ to $(-\infty, \infty)$ by taking $\alpha_j(t) = 0$ for $t < 0$. With this extension, we have $\hat{\alpha}_j(\omega) = \tilde{\alpha}_j(-i\omega)$. Note that

$$\frac{d^n\hat{\phi}}{d\omega^n} = \int_0^\infty e^{-i\omega t}(-it)^n \phi(t) dt.$$

Hence, if the nth derivative of the Fourier transform $\hat{\phi}$ exists, then ϕ decays no slower than $t^{-(n+1)}$. For instance, the slow decay of β can also be seen from its Fourier transform

$$\hat{\beta}(\omega) = 1 - \frac{\omega^2}{2} - \frac{i\omega}{2}\sqrt{4-\omega^2},$$

which contains a term $\sqrt{4-\omega^2}$ that has infinite derivative at $\omega = \pm 2$.

Based on this observation, we will continue the calculation in Fourier space. Taking Laplace transform of (3.14), we get

$$\sum_{j=1}^{J} \widetilde{\alpha_j}\tilde{\theta}^{-j} = 1, \tag{3.15}$$

in the Laplace/Fourier space. The idea is for $J > 1$, one can reduce the singularity in $\hat{\theta}$ by properly choosing the $\widetilde{\alpha_j}$'s. For that purpose we introduce the following functions,

$$R_n(s) = P_n(s^2) - s(s^2+4)^{n-\frac{1}{2}}.$$

Here P_n is a polynomial with degree n. It is chosen in such a way that,

$$\lim_{s\to+\infty} R_n(s) = 0.$$

This guarantees that the inverse Laplace transform can be applied. For example, $P_1(s^2) = 1 + s^2/2$ and $R_1(s) = \tilde{\theta}(s)$.

With the substitution $s = -i\omega$, we can see that $R_n(-i\omega) \in C^{n-1}$. So the corresponding inverse Fourier transform decays no slower than t^{-n}.

Next we rewrite (3.15) as,

$$\hat{\alpha}_J = \hat{\theta}^J - \sum_{j=1}^{J-1} \hat{\theta}^j \hat{\alpha}_{J-j}, \tag{3.16}$$

and we pick,

$$\tilde{\alpha}_j(s) = C_j R_{2J-j+1}, 0 < j < J. \tag{3.17}$$

With this choice, all the kernels except α_J decay no slower than t^{-J}. Notice that the right hand side of the equation (3.16) contains singular terms like $(4-\omega^2)^{k-\frac{1}{2}}$. The key idea is that in order for α_J to have decay rate J, we select the coefficient C_j in such a way that the singular terms for $1 \le k \le J-1$ are eliminated. This can be done by substituting (3.17) into (3.16), collecting the singular terms of the same order and setting up a linear system. Therefore the problem of finding α_J is reduced to solving the linear system of equations for C_js.

Following this procedure, for $J = 2$, we find,

$$\begin{aligned}
\alpha_1 &= \frac{J_0(2t)}{t^3}\big(-360+1440t^{-2}\big) + \frac{J_1(2t)}{t^2}\big(-60+1080t^{-2}-1440t^{-4}\big),\\
\alpha_2 &= \frac{-48J_0(2t)}{t^3} + \frac{J_1(2t)}{t^2}\big(-24+48t^{-2}\big),
\end{aligned}$$

and for $J = 3$ we find,

$$\begin{aligned}
\alpha_1 &= \frac{J_0(2t)}{t^3}\big(-420+332640t^{-2}-6400800t^{-4}+19051200t^{-6}\big)\\
&+ \frac{J_1(2t)}{t^4}\big(30240-1945440t^{-2}+15926400t^{-4}-19051200t^{-6}\big),\\
\alpha_2 &= \frac{J_0(2t)}{t^5}\big(20160-80640t^{-2}\big) + \frac{J_1(2t)}{t^4}\big(3360-60480t^{-2}+80640t^{-4}\big),\\
\alpha_3 &= \frac{J_0(2t)}{t^3}\big(240-1440t^{-2}\big) + \frac{J_1(2t)}{t^4}\big(-960+1440t^{-2}\big).
\end{aligned}$$

Similar results have been obtained for the case $J = 4$. These results suggest that in general, the kernels in (3.14) decay like $\mathcal{O}(t^{J+1/2})$. Hence by extending the stencil in space, one makes the boundary condition less history-dependent.

Numerically computing the exact time history kernels can be costly [6, 27, 32], especially for 3D crystals. Since they are *nonlocal in both space and time*, they are not the most efficient in actual simulations. It is therefore of practical interest to look for *local* boundary conditions. This becomes even more of an issue in multi-scale methods such as those in [10, 24], which bridge MD with continuum models, because in these methods the MD region can change in time. The main objective of this paper is to develop a systematic way of constructing *local* boundary conditions that are as effective as the exact boundary conditions, but more suitable for actual MD simulations.

3.2 Analysis of phonon reflection

We begin with a brief discussion on the discrete lattice waves – phonons. More detailed discussion can be found in standard solid state physics textbooks, for example [4]. The procedure is as follows. We first linearize the equations of motion (3.1) around the equilibrium state. We then apply normal mode analysis to obtain the phonon spectrum.

Let $\mathbf{r}_i$ and $\mathbf{R}_i$ be the equilibrium and deformed position of the i-th atom, respectively, and let $\mathbf{u}_i = \mathbf{R}_i - \mathbf{r}_i$ be the displacement vector. To study the phonon spectrum, we approximate the interatomic potential by its second order Taylor expansion,

$$V(\mathbf{R}_1, \mathbf{R}_2, \cdots, \mathbf{R}_N) = V_0 + \frac{1}{2}\sum_{i\neq j} \mathbf{u}_i^T D_{i-j} \mathbf{u}_j. \tag{3.18}$$

This is known as harmonic approximation. The force constants $\{D_j\}$ are related to the second order derivatives of the potential. For example, for potentials with only pairwise interaction,

$$V = \frac{1}{2}\sum_{i\neq j} \phi(r_{ij}), \quad r_{ij} = |\mathbf{r}_i - \mathbf{r}_j|$$

then (see [4])

$$D_j = \begin{cases} \sum_k \nabla^2\phi(r_{jk}), & j = 0, \\ -\nabla^2\phi(r_j), & j \neq 0. \end{cases} \tag{3.19}$$

Here $r_j = |\mathbf{r}_j|$.

This approximation leads to the linearized Newton's equation,

$$M\ddot{\mathbf{u}}_i = -\sum_j D_{i-j}\mathbf{u}_j. \tag{3.20}$$

We now introduce the dynamic matrix:

$$\mathcal{D}(\mathbf{k}) = \sum_j D_j e^{-i\mathbf{k}\cdot\mathbf{r}_j}, \tag{3.21}$$

In order for the crystal structure to be stable, the eigenvalues, λ_s, of the matrix $M^{-1}\mathcal{D}$ have to be nonnegative. The corresponding eigenvectors $\boldsymbol{\varepsilon}_s(\mathbf{k})$ are called the polarization vectors. We will use the standard normalization,

$$\boldsymbol{\varepsilon}_s \cdot \boldsymbol{\varepsilon}_{s'} = \delta_{ss'}. \tag{3.22}$$

Substituting the time harmonic function

$$\mathbf{u}_j = e^{i(\mathbf{k}\cdot\mathbf{r}_j - \omega_s t)}\boldsymbol{\varepsilon}_s(\mathbf{k}),$$

into (3.20), one finds the dispersion relation,

$$\omega_s^2 = \lambda_s.$$

We will take $\omega_s = \sqrt{\lambda_s}$. The index $1 \le s \le S$ designates the different phonon branch, and S is the number of branches in the spectrum. For simple lattice, $S = d$. To carry out the same analysis for a complex lattice with n_a atoms in each primitive cell, one can put together the displacement of all the atoms within each cell, and define an extended displacement vector,

$$\mathbf{u}_j = (\mathbf{u}_j^{(1)}, \mathbf{u}_j^{(2)}, \cdots, \mathbf{u}_j^{(n_a)}),$$

where the superscript indicates the order of the atoms in a primitive cell. This way the size of the dynamic matrix is $n_a d \times n_a d$, and $S = n_a d$.

The phonon spectrum inherits some symmetry properties from the original lattice. To see this, let P be a transformation in the space symmetry group of the lattice, and

$$\det(P) = \pm 1, P^T P = I.$$

Since the lattice is invariant under the transformation P, from (3.20) one has

$$P\mathcal{D}(\mathbf{k})P^T = \mathcal{D}(P\mathbf{k}). \tag{3.23}$$

Using (3.23), one gets,

$$\lambda_s(\mathbf{k}) = \lambda_s(P\mathbf{k}), \quad \boldsymbol{\varepsilon}_s(P\mathbf{k}) = P\boldsymbol{\varepsilon}_s(\mathbf{k}). \tag{3.24}$$

This shows that the polarization is altered by the transformation, while the phonon frequency remains unchanged.

We will use a wavenumber $\mathbf{k}$ to indicate a phonon mode. Due to the periodic structure of the lattice, some of the phonon modes are equivalent. For this reason, we restrict the wavenumber to the first Brillouin zone, denoted by B. Among the equivalent modes, the set B selects the one with smallest magnitude.

Now we study phonon reflection due to the applied boundary conditions. In particular we discuss how to find all the possible reflected phonons given an incident wave. In the context of elastodynamics, this issue has been previously studied both experimentally and theoretically [26, 29]. In order for the displacement and strain to be continuous before and after the phonon reflection, the frequency and the component of the wave vector parallel to the boundary have to be conserved. To be more specific, let $\mathbf{k}^I$ and $\mathbf{k}^R$ be the wavenumber corresponding to the incident and reflected phonon mode respectively, and $\mathbf{k}^I \in B$. Then $\mathbf{k}^R$ must satisfy,

$$\mathbf{k}^I - (\mathbf{k}^I \cdot \mathbf{n})\mathbf{n} = \mathbf{k}^R - (\mathbf{k}^R \cdot \mathbf{n})\mathbf{n}, \quad \omega_s(\mathbf{k}) = \omega_{s'}(\mathbf{k}^R), \tag{3.25}$$

for some $1 \le s, s' \le S$. This is schematically shown in Fig. 3. Also plotted are the level sets of the frequency, and the plane expressed by the first equation in (3.25). The intersections will determine the wavenumber of the reflected phonons.

A special case is when the reflected wave is on the same phonon branch as the incident wave, namely $s = s'$, then,

$$\mathbf{k}^R = \mathbf{k}^I - 2(\mathbf{k}^I \cdot \mathbf{n})\mathbf{n}, \tag{3.26}$$

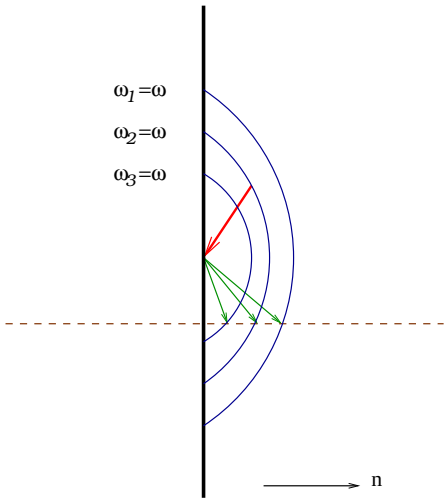

Figure 3: Schematics of incident and reflected waves. The case of one incident wave $\mathbf{k}^I$ and three resulting reflected waves is shown. We also drew the level sets of the phonon branches $\omega_s(\mathbf{k}) = \omega(\mathbf{k}^I), s = 1, 2, 3$, as well as the plane $\mathbf{k} - (\mathbf{k}\cdot\mathbf{n})\mathbf{n} = \mathbf{k}^I - (\mathbf{k}^I\cdot\mathbf{n})\mathbf{n}$ (dashed line). The intersections determine the wavenumber of the reflected waves.

satisfies (3.25) owing to the mirror symmetry of the phonon frequency with respect to the boundary.

Although equations (3.25) provide sufficient information for finding the reflected phonons, they are numerically difficult to solve. Here we provide an alternative procedure: we first make the following decomposition along the tangential and the normal directions of the boundary

$$\mathbf{k} = \mathbf{k}_t + (\mathbf{k}\cdot\mathbf{n})\mathbf{n}, \quad \mathbf{k}_t\cdot\mathbf{n} = 0.$$

In addition we let,

$$\lambda = e^{-i\mathbf{k}\cdot\mathbf{n}a_n}, \tag{3.27}$$

where a_n is the lattice spacing along the normal direction. For instance in Fig. 2, $a_n = a_0/2$ is half of the lattice parameter. Next we make the observation that along the normal direction, the crystal consists of layers. Therefore to compute the dynamic matrix, we can group all the terms that come from the same layer. In fact, we can define,

$$\hat{D}_l(\mathbf{k}_t) = \sum_{\mathbf{r}_j\cdot\mathbf{n}=la_n} D_j e^{-i\mathbf{k}_t\cdot\mathbf{r}_j}, \tag{3.28}$$

and after a Fourier transform along the normal direction, we have

$$\mathcal{D}(\mathbf{k}) = \sum_{l=-N_e}^{N_e} \hat{D}_l\lambda^l, \tag{3.29}$$

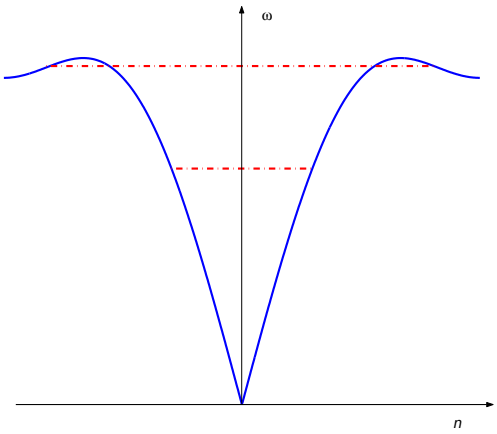

Figure 4: Selection of the wavenumbers that correspond to the reflected wave. For some fixed $\mathbf{k}_t$, we can plot the dispersion relation along the normal direction. In this example $S = 1, N_e = 4$. For low frequency ω, one finds two real and two complex solutions to (3.30). At high frequency, four real solutions can be found, two of which have positive group velocity, providing the wavenumber for the reflected phonons.

where N_e is the number of layers that have direct interactions with the outer-most layer.

This provides an alternative way of finding the reflected phonons: given an incident wave, we first compute the matrices (3.28) since $\mathbf{k}_t^R = \mathbf{k}_t^I$ is known. Next, to match the frequency of the incident and reflected phonons, we must have,

$$\det\left|\mathcal{D}(\mathbf{k}^R) - \omega_s^2(\mathbf{k}^I)I\right| = 0. \tag{3.30}$$

Clearly this leads to a polynomial with degree $2N_e \times S$. Meanwhile notice that $D_j = D_{-j}^T$. The transpose is only necessary for complex lattices. This, along with (3.28) implies that $\hat{D}_{-l} = \hat{D}_l^*$. Therefore the roots of (3.30) come in pairs: if λ is a solution, then $1/\overline{\lambda}$ is also a solution. Once all the roots are found, we obtain the normal components of the reflected phonon mode from (3.27).

Equation (3.30) should be satisfied by both the reflected and transmitted phonons. The selection of the wavenumbers that correspond to the reflected phonons is done in the following way: if the wavenumber is complex, then from the discussion above and from (3.30) and (3.27), we have a pair of wavenumbers $\mathbf{k} \cdot \mathbf{n} = a \pm bi$. In this case we choose the one with positive imaginary part which leads to a wave mode with exponentially decaying amplitude. On the other hand if the wavenumber is real, then because of crystal symmetry, we have a pair of wavenumbers $\mathbf{k} \cdot \mathbf{n} = \pm\xi$. In this case we choose the one with positive group velocity $\nabla_{\mathbf{n}}\omega > 0$. This corresponds to a wave packet that re-enters the domain after the reflection. This selection procedure is shown in Fig. 4.

We will denote these wave vectors as

$$\{\mathbf{k}_{ss'_l}^R, l = 1, 2, \cdots, N_R\}, \quad N_R = N_e \times S,$$

with s and s'_l indicating the branch of the incident and reflected phonon mode respectively.

Remark 3.1. It is likely that the wavenumber becomes complex. This happens, for instance, when the incident angle is large. It will be shown that the energy flux corresponding to these phonon mode vanishes along the normal direction. Therefore the energy will be trapped at the boundary and will not re-enter the domain.

Remark 3.2. There has been studies on phonon reflection in the context of linear elastodynamics [26,29]. In that case, the number of reflected waves is equal to the dimension. In the case of MD, the number of reflected phonons depends on the effective range of the atomic interaction and the number of phonon branches.

The wavenumber of the reflected phonon does not depend on the particular boundary condition. But the magnitude of the reflected wave does. In this paper we will focus on the following class of boundary conditions,

$$\mathbf{u}_0(t) = \sum_{\mathbf{r}_j \in J} \int_0^{t_0} \boldsymbol{\alpha}_j(\tau)\mathbf{u}_j(t-\tau)d\tau, \tag{3.31}$$

with the matrices $\left(\boldsymbol{\alpha}_j\right)_{d\times d}$ to be determined. The set J is a set of lattice points that correspond to some neighbors of atom 0 located inside the MD domain, namely $\mathbf{r}_j \cdot \mathbf{n} \geq 0, \forall \mathbf{r}_j \in J$. This is called the **stencil** in numerical analysis. We will use $|J|$ to indicate the number of atoms in this set.

These boundary conditions are clearly more general than those in (3.9). It offers the flexibility of choosing the stencil: the number of the neighboring atoms $|J|$ and the number of previous time steps involved. Our hope is that by using more atoms in space, we might get away with using less previous time steps.

To compute the reflection produced by the boundary condition (3.31), we consider linear superposition of an incident and the resulting reflected waves,

$$\mathbf{u}_j(t) = c_s^I e^{i(\mathbf{k}\cdot\mathbf{r}_j - \omega_s t)}\boldsymbol{\varepsilon}_s(\mathbf{k}) + \sum_{l=1}^{N_R} c_{ss'_l}^R e^{i(\mathbf{k}_{ss'_l}^R\cdot\mathbf{r}_j - \omega_s t)}\boldsymbol{\varepsilon}_{s'_l}(\mathbf{k}_{ss'_l}^R). \tag{3.32}$$

After substitution into (3.31), we find,

$$c_s^I\Big(I - \mathcal{A}(\mathbf{k})\Big)\boldsymbol{\varepsilon}_s(\mathbf{k}) + \sum_l c_{ss'_l}^R\Big(I - \mathcal{A}(\mathbf{k}_{ss'_l}^R)\Big)\boldsymbol{\varepsilon}_{s'_l}(\mathbf{k}_{ss'_l}^R) = 0,$$

where,

$$\mathcal{A}(\mathbf{k}) = \sum_j e^{i\mathbf{k}\cdot\mathbf{r}_j}\int_0^{t_0}\boldsymbol{\alpha}_j(\tau)e^{i\omega_s\tau}d\tau,$$

is reminiscent of a mixed Fourier and Laplace transform.

Next let $R_s = (R_{ss'_1}, R_{ss'_2}, \cdots, R_{ss'_{N_R}})$ be the solution of the linear system,

$$M_s^R R_s + M_s^I = 0, \tag{3.33}$$

where the s'_l-th column of the matrix M_s^R is

$$\Big(I - \mathcal{A}(\mathbf{k}^R_{ss'})(\mathbf{k})\Big)\boldsymbol{\varepsilon}_{s'_l}(\mathbf{k}^R_{ss'_l}),$$

and,

$$M_s^I = \Big(I - \mathcal{A}_s^I(\mathbf{k})\Big)\boldsymbol{\varepsilon}_s(\mathbf{k}).$$

Then the amplitudes of the reflected waves are given in terms of the amplitude of the incident wave by

$$c^R_{ss'_l} = R_{ss'_l} c^I_s,$$

for $1 \le s \le S$.

In the calculations above the boundary condition (3.31) for atom 0 has been used. For any other atom $\mathbf{r}_i$ on the same layer, since $\mathbf{r}_i \cdot \mathbf{n} = \mathbf{r}_0 \cdot \mathbf{n}$, the same results will follow if the following boundary condition is applied,

$$\mathbf{u}_i(t) = \sum_{\mathbf{r}_j - \mathbf{r}_i \in J} \int_0^{t_0} \boldsymbol{\alpha}_j(\tau)\mathbf{u}_j(t-\tau)d\tau. \tag{3.34}$$

The stencil for any other atom is obtained with a simple translation. As discussed before, there are N_e layers of boundary atoms for which boundary conditions have to be supplied. Similar boundary conditions can be sought for other layers. For practical purposes, we will apply the same boundary condition (3.34) to atoms on all other layers: $l = 0, 1, \cdots, N_e - 1$. This reduces the number of history kernels involved and makes the implementation easier. Different equations will be obtained from different layers following the same analysis and they will be added to (3.33). Since for each layer the matrix M_s^R has N_R columns and S rows, in total we obtain a N_R by N_R linear system, which can be solved for the reflection matrix R_s.

In practical implementations, we use a discrete version of (3.31):

$$\mathbf{u}_0^{n+1} = \sum_{j \in J} \sum_{m=1}^{M} \boldsymbol{\alpha}_j^m \mathbf{u}_j^{n-m+1} \Delta t, \tag{3.35}$$

where $\mathbf{u}_j^n$ approximates $\mathbf{u}_j(n\Delta t)$, and Δt is the time step in the MD simulation. M here indicates the number of time steps involved in the boundary condition. One can follow the same procedure and carry out similar analysis on the phonon reflection. The only major difference that enters the analysis is that the dispersion relation depends on the time step Δt. For example with velocity Verlet discretization,

$$\ddot{\mathbf{u}}_j \approx \frac{\mathbf{u}_j^{n+1} - 2\mathbf{u}_j^n + \mathbf{u}_j^{n-1}}{\Delta t^{\,2}},$$

the dispersion relation for the discrete MD equation,

$$\frac{\mathbf{u}_j^{n+1} - 2\mathbf{u}_j^n + \mathbf{u}_j^{n-1}}{\Delta t^{\,2}} = -\frac{\partial V}{\partial \mathbf{R}_j}, \tag{3.36}$$

is given by,

$$\omega_s = \frac{2}{\Delta t} \arcsin\big(\frac{\Delta t}{2}\sqrt{\lambda_s}\big). \tag{3.37}$$

3.3 Variational absorbing boundary conditions

Physically phonons are the carriers of thermal energy, and the propagation of phonons will result in energy transport. Phonon reflection is often observed with the increase of local temperature. It is therefore natural to formulate the boundary condition by minimizing the thermal flux, especially the component normal to the boundary. Starting from molecular dynamics at the atomic scale, we will express the energy flux due to phonon reflection in terms of the reflection coefficients R_s. For simplicity we will assume that the crystal is a simple lattice. Similar calculations, however, can be done for complex lattices.

In the harmonic approximation, the energy flux is expressed by,

$$J = -\frac{1}{2}\sum_{i\neq j}(\dot{\mathbf{u}}_{\mathbf{r}_i} + \dot{\mathbf{u}}_j)^T D_{i-j}(\mathbf{u}_i - \mathbf{u}_j)\mathbf{r}_{ij}. \tag{3.38}$$

The formula was derived from the energy balance at the atomic scale [21, 24]. The energy flux normal to the boundary, $J \cdot \mathbf{n}$, is directly responsible for the energy change in the system.

The double summation can be rewritten in terms of the position of all atoms $\mathbf{r}_i$ and their neighbors $\mathbf{r}_i + \mathbf{r}_j$,

$$J = -\frac{1}{2}\sum_i\sum_j(\dot{\mathbf{u}}_i + \dot{\mathbf{u}}_{i-j})^T D_j(\mathbf{u}_i - \mathbf{u}_{i-j})\mathbf{r}_j. \tag{3.39}$$

Now notice that the summation over i and j can be interchanged. We will transform the summation over $\mathbf{r}_i$ to Fourier space and keep the summation over $\mathbf{r}_j$. Meanwhile we will take the Fourier representation (3.32) of $\mathbf{u}_i$ and proceed with the calculation for the energy flux on each phonon branch, denoted by J_s for the sth branch.

Using Plancherel's theorem, we obtain

$$J_s = -\frac{1}{2}\sum_j \int i\omega_s \mathbf{u}^*(\mathbf{k})D_j\mathbf{u}(\mathbf{k})\big(1 + e^{i\mathbf{r}_j\cdot\mathbf{k}}\big)\big(1 - e^{-i\mathbf{r}_j\cdot\mathbf{k}}\big)d\mathbf{k}\ \mathbf{r}_j.$$

Substituting (3.32) into the integral, and noticing that the wavenumber of the incident and reflected phonons have different normal components, we can split the integral,

$$J_s = J_s^I + J_s^R,$$

with,

$$J_s^I = \sum_j \int |c_s^I|^2 \omega_s \boldsymbol{\varepsilon}_s^*(\mathbf{k}) D_j \boldsymbol{\varepsilon}_s(\mathbf{k}) \sin(\mathbf{k}\cdot\mathbf{r}_j) d\mathbf{k}\,\mathbf{r}_j,$$

$$J_s^R = \sum_j \sum_l \int |c_s^R|^2 \omega_s \boldsymbol{\varepsilon}_{s_l'}^*(\mathbf{k}_{ss_l'}^R) D_j \boldsymbol{\varepsilon}_s(\mathbf{k}_{ss_l'}^R) \sin(\mathbf{k}_{ss_l'}\cdot\mathbf{r}_j) d\mathbf{k}\,\mathbf{r}_j,$$

representing respectively the energy flux due to the incident and reflected waves. The Sine function comes from the calculation of,

$$(1+e^{i\mathbf{k}\cdot\mathbf{r}})(1-e^{-i\mathbf{k}\cdot\mathbf{r}}).$$

We first discuss the case where the wavenumber $\mathbf{k}$ of a reflected phonon has a complex normal component. Using the identity,

$$\sin(a+bi) + \overline{\sin(a+bi)} = 2\cosh(b)\sin(a),$$

we find that

$$\phi_j(\mathbf{k}) + \overline{\phi_j}(\mathbf{k}) + \phi_{-j}(\mathbf{k}) + \overline{\phi_{-j}}(\mathbf{k}) = 0,$$

where the function ϕ,

$$\phi_j(\mathbf{k}) = \sin(\mathbf{k}\cdot\mathbf{r}_j)\mathbf{r}_j\cdot\mathbf{n}.$$

Therefore these waves do not contribute to normal component of the energy flux. They are surface waves. In the following calculation we will assume that the wavenumber is always real.

Next let k_α and r_j^α be the αth components of the vectors $\mathbf{k}$ and $\mathbf{r}_j$ respectively. Notice that,

$$\mathcal{D}(\mathbf{k}) = \sum_{\mathbf{r}_j} D_j\big(2-2\cos(\mathbf{k}\cdot\mathbf{r}_j)\big),$$

therefore,

$$2\sum_{\mathbf{r}_j} D_j \sin(\mathbf{k}\cdot\mathbf{r}_j) r_j^\alpha = \nabla_{k_\alpha}\mathcal{D}(\mathbf{k}),$$

gives the directional derivative. On the other hand,

$$\frac{d}{dk_\alpha}\mathcal{D}(\mathbf{k})\boldsymbol{\varepsilon}_s(\mathbf{k}) = \frac{d}{dk_\alpha}\lambda_s(\mathbf{k})\boldsymbol{\varepsilon}_s(\mathbf{k}) - \big(\mathcal{D}(\mathbf{k})-\lambda\big)\frac{d}{dk_\alpha}\boldsymbol{\varepsilon}_s(\mathbf{k}).$$

The last term drops out when multiplied by $\boldsymbol{\varepsilon}_s(\mathbf{k})^*$ from the left.

Finally using equation (3.22), we have,

$$J_s^I\cdot\mathbf{n} = \int |c_s^I|^2\omega_s^2\nabla\omega_s(\mathbf{k})\cdot\mathbf{n}\,d\mathbf{k}.$$

Similarly,

$$J_s^R\cdot\mathbf{n} = \sum_l \int |c_{ss_l'}^R|^2\omega_s^2\nabla\omega_{s_l'}(\mathbf{k}_{ss_l'}^R)\cdot\mathbf{n}\,d\mathbf{k}_{ss'}^R.$$

This is consistent with the observation that the energy is transported at group velocity.

To simplify the second integral, we switch the variables $\mathbf{k}^R_{ss'_l}$ to $\mathbf{k}$ and change the integral to half of the Brillouin zone where $\mathbf{k}\cdot\mathbf{n}\leq 0$. The Jacobian is obtained from (3.25),

$$\frac{\partial\tilde{\mathbf{k}}^R_{ss'_l}}{\partial\mathbf{k}}=\frac{\partial_{\mathbf{n}}\omega_s}{\partial_{\mathbf{n}}\omega_{s'}}.$$

Therefore the energy flux due to phonon reflection can be expressed as,

$$J^R\cdot\mathbf{n}=\sum_s\int_{\mathbf{k}\in B,\,\mathbf{k}\cdot\mathbf{n}\leq 0}|\sum_l c_s^I R_{ss'_l}|^2\omega_s^2\,|\nabla\omega_s\cdot\mathbf{n}|d\mathbf{k}. \tag{3.40}$$

Absolute value is used for the group velocity because the reflected phonon mode has positive group velocity along the normal direction.

This calculation clearly shows the role of the reflection matrix in the energy flux. It also suggests that in order to minimize phonon reflection, it is natural to choose the coefficients such that $J^R\cdot\mathbf{n}$, the energy flux due to phonon reflection off the boundary, is minimized.

Equations (3.33), (3.34) and (3.40) constitute the basis for constructing a boundary condition for MD. Specifically, we will choose the time history kernels by minimizing the total reflection. We first define the objective function,

$$I\big[\{\boldsymbol{\alpha}_j\};\mathbf{n}\big]=\sum_s\int_{\mathbf{k}\in B,\,\mathbf{k}\cdot\mathbf{n}\leq 0}\sum_l|R^2_{ss'_l}|\,|\nabla\omega_s\cdot\mathbf{n}|d\mathbf{k}. \tag{3.41}$$

The term $|c_I|^2\omega^2$ has been replaced by a constant, which represents the case with uniform phonon distributions. We then consider the variational problem,

$$\min I\big[\{\boldsymbol{\alpha}_j\};\mathbf{n}\big], \tag{3.42}$$

subject to certain constraints. The boundary condition (hereafter referred to as VBC) is optimal in that it leads to minimal phonon reflection given a stencil.

It is also possible to choose the total reflection [11, 12] as the objective function,

$$\int_{\mathbf{k}\in B,\,\mathbf{k}\cdot\mathbf{n}\leq 0}\sum_s\sum_l|R_{ss'_l}|^2d\mathbf{k}. \tag{3.43}$$

One concern here is that the reflection may have finite values at points where the group velocity vanishes [11, 12].

Constraints. The above formalism uses the group velocity as weight for different wavenumbers. In order to guarantee the desired accuracy at large scale, we can impose as explicit constraints that phonon reflection vanishes at small $\mathbf{k}$. For example, for the acoustic branches for which $\omega_s(0)=0$, we require that

$$\lim_{\mathbf{k}\to 0}M_s^I(\mathbf{k})=0.$$

This gives,

$$\sum_j \int_0^{t_0} \boldsymbol{\alpha}_j(\tau) d\tau = I, \tag{3.44}$$

which can also be viewed as the condition of Galilean invariance. In addition we may require that the directional derivative,

$$\frac{\partial}{\partial \boldsymbol{\xi}} M_s^I,$$

along certain direction $\boldsymbol{\xi}$ go to zero. For example we can take $\boldsymbol{\xi} = -\mathbf{n}$, the normal incidence. This leads to,

$$\sum_j \int_0^{t_0} \boldsymbol{\alpha}_j(\tau) \tau d\tau \; \partial_{\boldsymbol{\xi}} \omega_s(0) \boldsymbol{\varepsilon}_s + \sum_j \int_0^{t_0} \boldsymbol{\alpha}_j(\tau) d\tau \mathbf{r}_j \cdot \boldsymbol{\xi} \boldsymbol{\varepsilon}_s = 0. \tag{3.45}$$

One may impose certain additional constraints in order to respect the symmetry of the crystal. This will be explained in section 4.2.

Finally we discuss the numerical implementation. First we need to discretize the first Brillouin zone to compute the total reflection. We have used the traditional K-point method [16,25]. In this method, we first generate the grid points in the wavenumber space by,

$$\boldsymbol{\xi}_{l,m,n} = \frac{2l - n_q + 1}{2n_q} \mathbf{k}_1 + \frac{2m - n_q + 1}{2n_q} \mathbf{k}_2 + \frac{2n - n_q + 1}{2n_q} \mathbf{k}_3,$$

where n_q is the number of grid points in each direction. We then move these grid points into the first Brillouin zone. Using the point-group symmetry of the grid points, one can significantly reduce the summation over the first Brillouin zone [25].

The optimization is done using the BFGS method [33]. To initiate the BFGS subroutine, we start with the kernels,

$$\boldsymbol{\alpha}_j^m = \begin{cases} \delta_{m1}/\Delta t, & \text{if } j = 0, \\ 0, & \text{otherwise.} \end{cases}$$

This amounts to fixing the displacement of the boundary atoms.

Here is a summary of the proposed procedure for finding the kernels of VBC:

1. Generate grid points in the first Brillouin zone.
2. Compute the dispersion relation and the polarization vectors at each grid point.
3. For each grid point $\mathbf{k}$, such that $\mathbf{k} \cdot \mathbf{n} \leq 0$, find all the possible wavenumbers for the reflected phonon: $\{\mathbf{k}_{ss_l'}^R, l = 1, 2, \cdots, N_R\}$, as well as the corresponding polarization vectors.
4. Select the stencil, i.e. the set J and the number of time steps M.
5. Initialize the time history kernels $\{\boldsymbol{\alpha}_j^m\}$.
6. Compute the reflection coefficients $R_{ss_l'}$ from equation (3.33) and the objective function from (3.41).
7. Use the BFGS subroutines to obtain new values for the time history kernels.

8. Go to step 6 unless certain convergence criterion is met.

To implement these boundary conditions in a MD simulation, one first needs to identify the boundary atoms, and for each boundary atom i, one finds the stencil such that $\mathbf{r}_j - \mathbf{r}_i \in J$. At each step of the time integration, the boundary condition (3.34) supplies the displacement of each boundary atom, and the forces exerted on the atoms inside are then computed which can be used by a time integrator to evolve the system to the next time step.

3.4 Examples

Here we provide a few examples to illustrate how VBC might be obtained. Clearly the computational cost of applying these boundary conditions depend on the size of the stencil $|J|$ and the number of time steps M. We will look at the total reflection and the time history kernels for different choice of J and M. For most the numerical tests we will choose the boundary atom itself as the first element in the set J.

3.4.1 1D linear chain

Our first example is the one dimensional chain considered earlier (3.10). The dispersion relation is given by

$$\omega^2 = 4\sin^2\frac{k}{2},\ k \in [-\pi, \pi). \tag{3.46}$$

We will consider the time-continuous case, and we will restrict our attention to boundary conditions of the form:

$$u_0 = \sum_j \int_0^{t_0} \alpha_j(\tau) u_j(t-\tau) d\tau. \tag{3.47}$$

The reflection coefficient can be found easily as (also see [11, 12]),

$$R(k) = \frac{1 - \sum_j e^{ijk} \int_0^{t_0} \alpha_j(\tau) e^{i\omega\tau} d\tau}{1 - \sum_j e^{-ijk} \int_0^{t_0} \alpha_j(\tau) e^{i\omega\tau} d\tau} \tag{3.48}$$

for k in the interval $[-\pi, 0]$, the left half of the first Brillouin zone. In particular, if we restrict the stencil to $\{j = 1, t_0 = +\infty\}$ and enforce zero reflection, we have

$$\widehat{\alpha_1} = e^{-ik} = 1 - \frac{\omega^2}{2} - \frac{i\omega}{2}\sqrt{4-\omega^2},$$

using (3.46). Taking the inverse Laplace transform, the exact boundary condition (3.12) is recovered.

Next we turn to the VBC. We will choose $J = \{1\}$ and compute the history kernels for $M = 500, 1000, 2000$ with constraints (3.44) and (3.45). In Fig. 5, we show the kernels computed from the variational problem in comparison with the exact kernel (3.12). One can clearly see that as we increase t_0, the computed kernel for VBC converges to the one for the exact boundary condition.

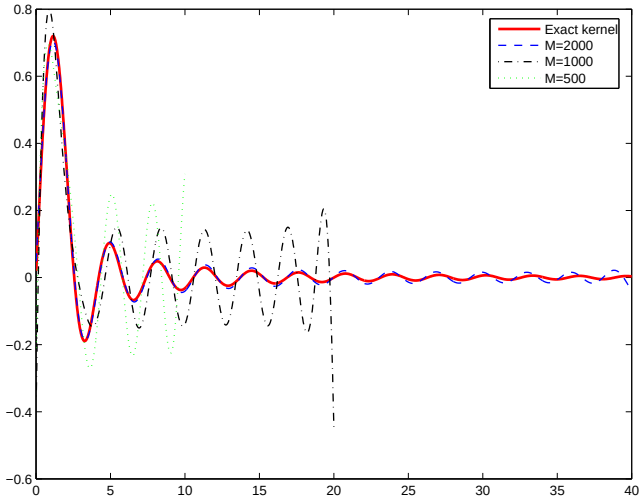

Figure 5: Exact kernel and the kernel obtained from the variational model. The x axis indicates time.

Despite the fact that the exact boundary condition can be found analytically, in actual computations they have to be truncated at some cut-off value, t_c [6, 32]. The slow decay of these kernels means that one has to choose rather large values of t_c. A premature truncation can lead to large reflection, as shown in Fig. 6 where reflection coefficients for the case $t_c = 4.0$ is shown. One can see large reflections near $k = 0$ and $k = \pi$. In comparison, the variational boundary condition using the same amount of history data gives much less reflection. More examples can be found in the work of E and Huang [11, 12] in which a simplified boundary conditions were developed that maximize the accuracy at the large scale and minimize the total reflection of phonon at the small scale. These boundary conditions have been used in a coupled atomistic-continuum scheme and applied successfully to model dislocation dynamics [12].

3.4.2 2D triangular lattice

Our second example is a 2D triangular lattice with the Lennard-Jones potential,

$$V = \sum_{i \neq j} \phi(r_{ij}),$$

where

$$\phi(r) = 4\epsilon\Big(\big(\frac{\sigma}{r}\big)^{12} - \big(\frac{\sigma}{r}\big)^{6}\Big),$$

with a cut-off radius $r_c = 1.7\sigma$. Since σ and ϵ can be used as the length and energy unit, they are taken to be unity in our computation. Meanwhile let m be the mass unit, then the unit for time is $\sigma\sqrt{m/\epsilon}$, the reciprocal of which gives the unit for the frequency. In our calculations, we have taken the time step $\Delta t = 0.01$, and $n_q = 32$ for the Brillouin zone integration. Experiments have been done which confirms that this is a stable time discretization for this MD system.

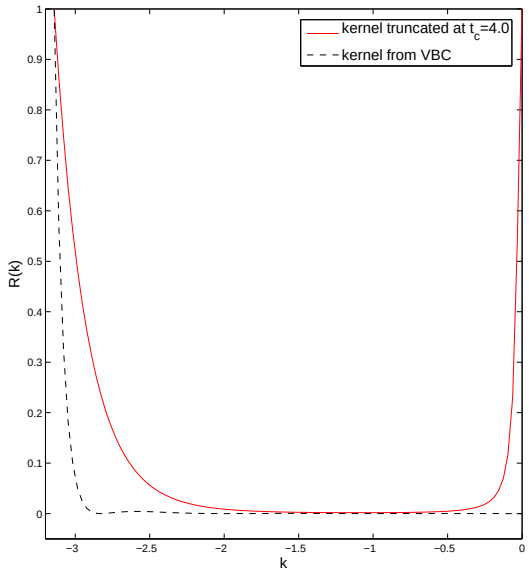

Figure 6: Reflection coefficients due to the applied boundary conditions. Dashed line: using the kernel (3.12) truncated at $t_c = 4.0$; solid line: using a kernel obtained from the variational boundary condition with the same time interval.

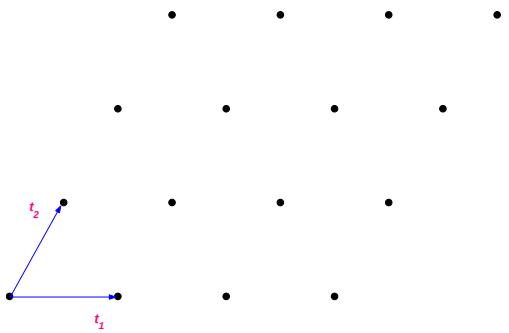

Figure 7: 2D triangular lattice for Lennard-Jones crystal.

The triangular lattice is generated from a primitive cell as indicated in Fig. 7. The basis for the primitive cell is,

$$\mathbf{t}_1 = (a_0, 0), \qquad \mathbf{t}_2 = (\frac{a_0}{2}, \frac{\sqrt{3}a_0}{2}), \tag{3.49}$$

where $a_0 = 1.122462\sigma$ is the lattice constant obtained by relaxing the crystal to equilibrium. The corresponding basis in the reciprocal space is,

$$\mathbf{k}_1 = \frac{2\pi}{V_0}(\frac{\sqrt{3}a_0}{2}, -\frac{a_0}{2}), \qquad \mathbf{k}_2 = \frac{2\pi}{V_0}(0, a_0), \tag{3.50}$$

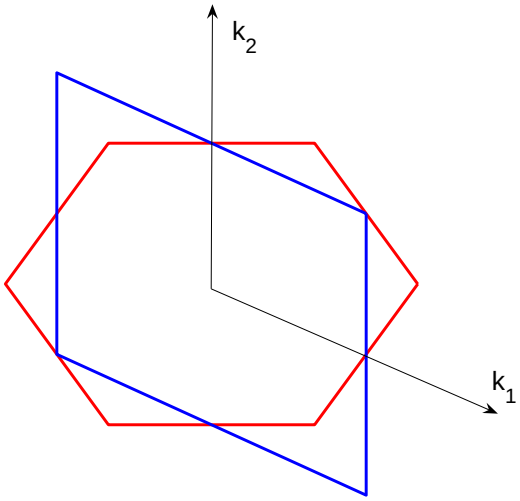

Figure 8: The first Brillouin zone and one particular unit cell for the 2D triangular lattice.

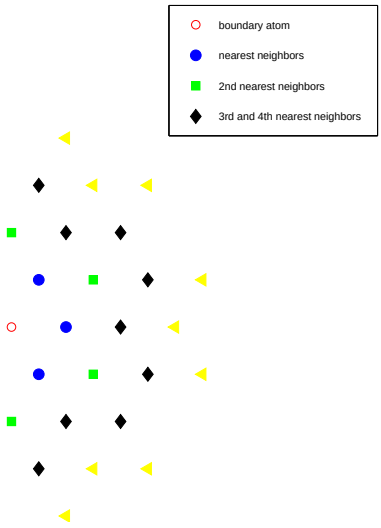

Figure 9: The neighboring atoms for a boundary atom. We plotted some neighboring lattice points which can be chosen to set up the stencil J.

where $V_0 = \frac{\sqrt{3}a_0^2}{2}$ is the volume of the primitive cell. With this choice the first Brillouin zone is a hexagon as shown in Fig. 8. Also plotted is a particular unit cell of the reciprocal lattice in the wavenumber space.

This lattice has been considered in [27], in which the exact boundary condition was found and expressed in terms of the displacement of the first two layers of atoms next to the boundary for all previous time. The great advantage of our boundary conditions is that it offers the

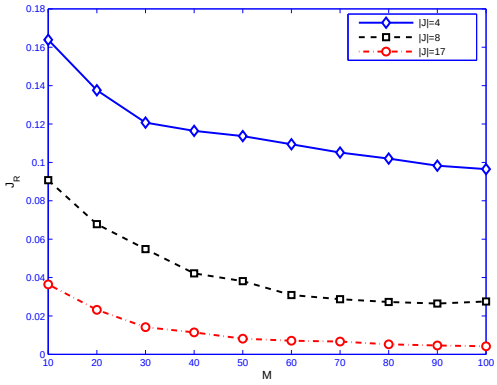

Figure 10: The total energy flux produced from the variational boundary conditions on various stencils.

flexibility of choosing the stencils, which are not necessarily within the first two layers. The way we select the stencil J is shown in Fig. 9: we plot the neighbors of a boundary atom in the case of $\mathbf{n} = (1, 0)$. For example we can choose the lattice points that correspond to the nearest neighbors, which gives four atoms including itself, or we may include both the first and the second nearest neighbors, which adds four more atoms in the stencil. In this case the stencil has been extended to some lattice points on the third layer.

To see the performance of different stencils, we conduct three sets of experiments for $|J| = 4$ $|J| = 8$, and $|J| = 17$ which corresponds to selecting the third and fourth nearest neighbors. This is again shown in Fig. 9. In each case the number of time steps M used in the boundary condition ranges from $M = 10$ to $M = 100$. The results are displayed in Fig. 10, where we plot the energy flux $J^R \cdot \mathbf{n}$. Clearly a larger stencil leads to less reflected energy flux. Fig. 10 also suggests that larger stencil in space is more efficient in absorbing the phonons than using longer time interval, for the same amount of data used. For example the stencil $\{|J| = 17, M = 30\}$ produces less reflection than the stencil $\{|J| = 8, M = 100\}$.

Fig. 10 also shows that the total reflection decays as the number of time steps is increased. Close inspection reveals that the decay rate for the three cases is approximately 0.5, 1.0 and 2.0 respectively. The suggests that as one extends the stencil, the corresponding total reflection tends to decay faster.

In Fig. 11, we show the surface plot of the reflection coefficient as a function of the wavenumbers on the left half of the Brillouin zone for the case $\{|J| = 8, M = 30\}$ and for the top branch $s = 1$. One can see that for most wavenumbers, the reflection is quite small. But two peaks are observed along the edges. This is because at these locations, the normal derivatives $\nabla_{\mathbf{n}}\omega$ of the frequency are small, which give small weight to the objective function.

Finally, to see how the kernels in VBC look like, we plot the $(1, 1)$ component in $\boldsymbol{\alpha}_1(t)$ in Fig. 12 with the lattice point $\mathbf{r}_1 = (a_0/2, a_0\sqrt{3}/2)$ for the case $|J| = 4$. Even with $M = 200$, no substantial decay is observed. Now we extend the stencil to $|J| = 11$ to include the second and third nearest neighbors, and plot the same memory kernel in the figure. Clearly with this choice the kernel has smaller amplitude at large time.

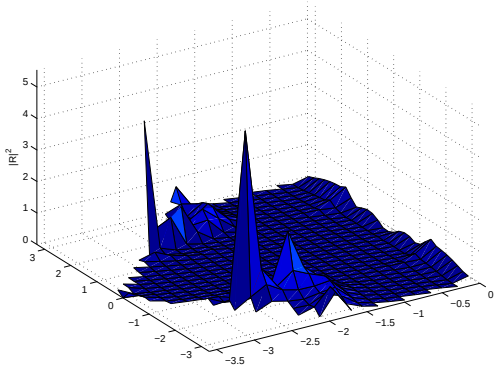

Figure 11: The total reflection $|R_s(k_1,k_2)|^2$ plotted on the left half of the Brillouin zone for the lower branch $s=2$. The stencil includes 8 atoms: $|J|=8$, and 30 time steps: $M=30$. In this picture, x axis is $\mathbf{k}=(1,0)$ and y axis is $\mathbf{k}=(0,1)$.

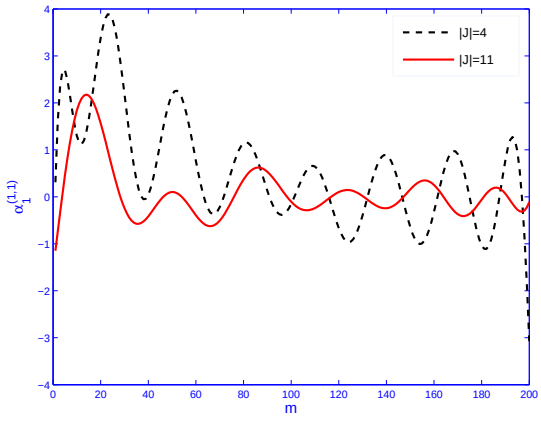

Figure 12: The time history kernel for $\boldsymbol{\alpha}_1(t)$ in the cases $|J|=4, M=200$ and $|J|=11, M=200$.

3.4.3 3D BCC lattice

For the body-centered cubic (BCC) lattice, we choose the standard basis,

$$\mathbf{t}_1=(\frac{a_0}{2},\frac{a_0}{2},-\frac{a_0}{2}),\quad \mathbf{t}_2=(-\frac{a_0}{2},\frac{a_0}{2},\frac{a_0}{2}),\quad \mathbf{t}_3=(\frac{a_0}{2},-\frac{a_0}{2},\frac{a_0}{2}).$$

The reciprocal lattice has the structure of a face-centered cubic (FCC) lattice. Again we consider the boundary with normal vector $\mathbf{n}=(1,0,0)$ and focus on the particular boundary atom placed at the origin. For the stencil, one may choose to include the lattice points,

$$(\frac{a_0}{2},\pm\frac{a_0}{2},\pm\frac{a_0}{2}),$$

for the nearest neighbors. In this case $|J| = 5$. Clearly the stencil is invariant under $\pm\pi/2$ and π rotation around the normal direction. From the discussion in section 4.2, it is then only necessary to obtain the kernel in the VBC for one of the four atoms. The second nearest neighbors would include lattice points at $(0, \pm a_0, \pm a_0)$ and $(a_0, 0, 0)$, and this adds five more atoms in the stencil. The atomistic model being used here is the Embedded Atom Model (EAM) developed in [28]. The lattice parameter predicted by this model is $a_0 = 2.8663\mathring{A}$ with cut-off radius $r_c = 4.0954\mathring{A}$. In this case $N_e = 4$ because $a_0 < r_c < \frac{3a_0}{2}$. Force constants have been analytically computed from this potential to determine the phonon spectrum. The length and energy unit in this model is Angstrom and Kelvin (multiplied by the Boltzmann constant) respectively. We will rescale the mass of an atom to unity, so the mass unit is 55.85 amu. This determines the time unit of the system, which is about 8.196ps. In all of our calculations, we take $\Delta t = 0.002$ which gives a stable time discretization. For the integration over the first Brillouin zone, $n_q = 16$.

In Fig. 14 we plot the kernels in the VBC for the 5th point in the stencil $\mathbf{r}_5 = \frac{a_0}{2}(1, 1, 1)$ for the case $|J| = 10$ and $M = 50$. In addition, we show in Fig. 15 the total reflection along the cross section (001). The overall behavior resembles what we found for the previous example.

3.4.4 2D graphene sheet

Our last example is the graphene sheet in the zigzag orientation shown in Fig. 16. This is a very interesting case: the displacement of each atom is a three dimensional vector. However the lattice is a two dimensional complex lattice consisting of two triangular lattices with lattice parameter a_0 and basis vectors $(\sqrt{3}a_0/2, \pm a_0/2)$. In each primitive cell there are two atoms, and the coordinate of the second atom relative to the first one is $(\sqrt{3}a_0/6, a_0/2)$. The first Brillouin zone is again a hexagon but with vertices located at $\pi/6, \pi/2, \cdots, 11\pi/6$ angles. The exact boundary condition for graphene has been derived by Wagner, Karpov and Liu [32]. One major difference here is that the boundary condition (3.31) is not expressed in terms of the extended displacement vector. Therefore the history kernels are 3-by-3 matrices, while in [32] they are 6-by-6.

The force constants have been computed numerically from the Tersoff potential [30]. The lattice parameter predicted by this model is $a_0 = 2.5288\mathring{A}$. The energy unit is electron volt. The time unit is about 0.03527ps. We choose the time step $\Delta t = 0.05$ and $n_q = 32$. Because there are two atoms in each primitive cell, the size of the dynamic matrix is 6-by-6, and in the phonon spectrum, there are 3 acoustic and 3 optical branches. Since only nearest neighbor interaction is present in the Tersoff's model, $N_e = 2$ and we only need to find boundary conditions for one layer of atoms. Again we focus on the boundary atom at the origin.

We first select points in the lattice corresponding to the nearest neighbors to form the set J. In this case $|J| = 3$ with $\mathbf{r}_1, \mathbf{r}_2 = (\frac{\sqrt{3}}{6}, \pm\frac{1}{2})a_0$. We first plot the total reflection for the top optical branch $s = 1$ with the number of time steps $M = 50$. Peaks are observed at the two vertices along the vertical axis. Again this is because the normal derivatives $\nabla_{\mathbf{n}}\omega$ are small at these points. Finally we plot the diagonal entries in the kernel $\boldsymbol{\alpha}_1$ in Fig. 18 for the case $|J| = 5$ and $M = 50$. In this case we extended the stencil to include the lattice points $\mathbf{r}_3, \mathbf{r}_4 = (\frac{\sqrt{3}}{2}, \pm\frac{1}{2})a_0$. One can see that the $(3, 3)$ entry of $\boldsymbol{\alpha}_1$ is much smaller the other two entries.

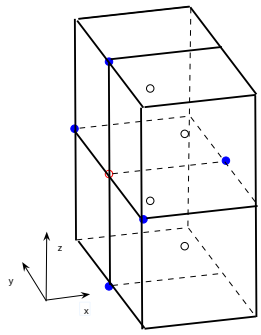

Figure 13: The stencil for BCC lattice. Open circles: the boundary atom and its nearest neighbors; filled circles: second nearest neighbors. The boundary coincides with the (100) plane: $\mathbf{n} = (1, 0, 0)$.

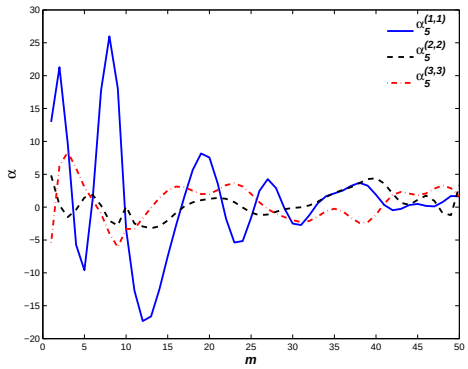

Figure 14: The time history kernels in the VBC for the BCC lattice: $n = (1, 0, 0)$, $|J| = 10$, and $M = 50$.

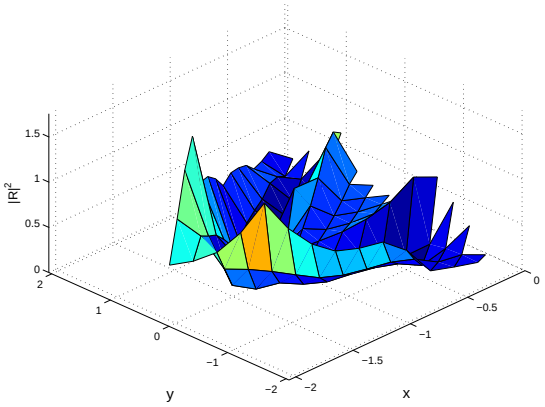

Figure 15: The reflection coefficient $|R_1|^2$ on the cross section (001).

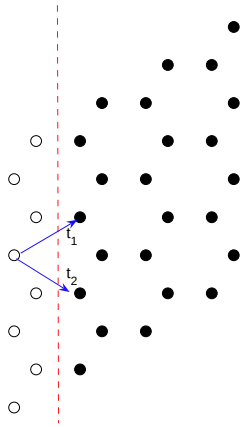

Figure 16: The lattice structure of graphene in the zigzag orientation. The boundary coincides with a plane shown in the figure with a dashed line. The arrows indicate the basis vectors. In our calculations, we took the first column of atoms from the left as the boundary atoms.

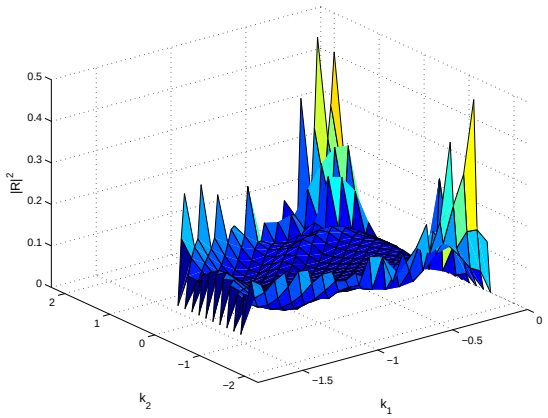

Figure 17: The reflection matrix plotted on the left half of the first Brillouin zone. x axis: $\mathbf{k} = (1, 0)$; y axis: $\mathbf{k} = (0, 1)$.

4 Implementations

Here we explain in more detail some of the steps in the numerical procedure for finding the kernels in the VBC.

4.1 Calculation of force constants

As input parameters, we need to obtain the force constants

$$D_{i-j} = \frac{\partial^2 V}{\partial \mathbf{x}_j \partial \mathbf{x}_i},$$

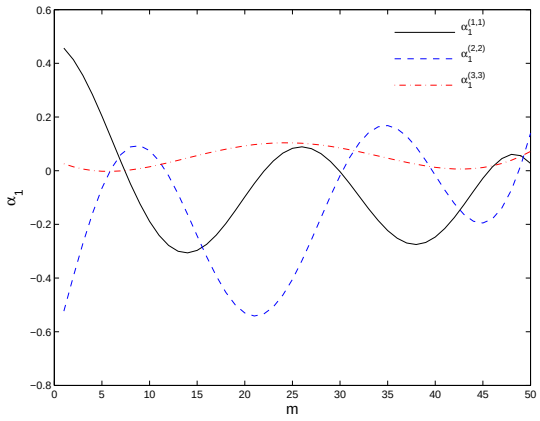

Figure 18: Some components of the kernel $\boldsymbol{\alpha}_1(t)$ for $|J| = 5$ and $M = 50$.

which are involved in the calculation of the dynamic matrix (3.21). Obtaining these force constants is a standard procedure used in computing phonon spectrum. For some models, such as pair potentials, and embedded atom models (EAM) [9], these matrices can be obtained analytically. In general, one has to rely on finite difference approximation. We will briefly illustrate the procedure below.

We start with a uniform state with all atoms at their equilibrium positions:

$$\mathbf{u}_j = 0, \text{and } f_j = -\frac{\partial V}{\partial x_j} = 0.$$

Now we displace the jth atom by $\delta\mathbf{u}$, which induces force $\delta\mathbf{f}$ on a selected atom, called the zeroth atom. Then we approximate the (α, β) entry of the matrix D_j by,

$$D_j^{(\alpha,\beta)} \approx -\frac{\delta\mathbf{f}^{(\beta)}}{\delta\mathbf{u}^{(\alpha)}}.$$

This procedure will be conducted for all the atoms that have direct interaction with the zeroth atom. Additional symmetry can be used to further reduce the number of matrices that need to be computed if the force calculation, e.g. in *ab initio* methods, is expensive [23].

4.2 Symmetry property of the history kernels

It is of practical convenience to transfer the kernels in (3.31) to a boundary on another equivalent plane. For example in the 2D lattice in Fig. 2, lines that differ by a rotation of multiples of $\pi/3$ are equivalent. Let $\mathbf{n}'$ be the normal to the new boundary, and P be the corresponding transformation within the symmetry group, $P\mathbf{n} = \mathbf{n}'$. Let $\mathbf{r}'_j = P\mathbf{r}_j$. We now look at the

reflection coefficient: $R\big(\mathbf{k};\{\boldsymbol{\alpha}_j\}\big)$. From (3.24), we have,

$$\begin{aligned} & A_s^I(P^T\mathbf{k})\boldsymbol{\varepsilon}_s(P^T\mathbf{k}) \\ = & \sum_j \int \boldsymbol{\alpha}_j(\tau) e^{i(\mathbf{r}_j\cdot P^T\mathbf{k}+\omega_s\tau)} d\tau P^T\boldsymbol{\varepsilon}_s(\mathbf{k}), \\ = & \sum_{j'} \int \boldsymbol{\alpha}_j(\tau) e^{i(\mathbf{r}_{j'}\cdot\mathbf{k}+\omega_s\tau)} d\tau P^T\boldsymbol{\varepsilon}_s(\mathbf{k}). \end{aligned}$$

This suggests that if we take,

$$\boldsymbol{\alpha}_{j'} = P\boldsymbol{\alpha}_j P^T, \tag{4.1}$$

we would have,

$$P^T M_s^I(\mathbf{k};\{\boldsymbol{\alpha}_{j'}\}) = M_s^I(P^T\mathbf{k};\{\boldsymbol{\alpha}_j\}).$$

Similarly we find,

$$P^T M_s^R(\mathbf{k};\{\boldsymbol{\alpha}_{j'}\}) = M_s^R(P^T\mathbf{k};\{\boldsymbol{\alpha}_j\}),$$

which leads to,

$$R_s\big(\mathbf{k};\{\boldsymbol{\alpha}_{j'}\}\big) = R_s\big(P^T\mathbf{k};\{\boldsymbol{\alpha}_j\}\big). \tag{4.2}$$

This implies that

$$I[\{\boldsymbol{\alpha}_{j'}\};\mathbf{n}'] = I[\{\boldsymbol{\alpha}_j\};\mathbf{n}].$$

Meanwhile the relation (4.1) preserves the constraints (3.44) and (3.45). This shows that if the set of kernels $\{\boldsymbol{\alpha}_j\}$ is optimal for the plane with normal $\mathbf{n}$, $\{\boldsymbol{\alpha}_{j'}\}$ is optimal for the new plane.

In particular if P maps the set of neighboring atoms to themselves, the above calculation shows that the special choice (4.1) leads to the symmetry of the reflection matrix in the first Brillouin zone. This is of some practical interest: on one hand, using the symmetry (4.1) as additional constraints, one can reduce the number of variables in the variational problem; numerous experiments have suggested that the symmetry constrains substantially speed up the iterations in the optimization procedure. On the other hand, with the additional symmetry of the reflection matrix, the cost of numerical integration over the Brillouin zone can be greatly reduced [16].

4.3 External loading

The boundary conditions we have discussed so far can be viewed as free boundary condition, i.e. with no external loading. Here we will consider the situation when external loading is added. Similar issues arise when designing hybrid atomistic-continuum methods. At the atomistic-continuum interface, one must supply boundary conditions for the atomistic system using information from the continuum calculations, in order to mimic the effect of the atoms that have been removed from the system. The information from the continuum region is often in the form of constraints on the displacement, strain or the stress for the boundary atoms. The issue is how to maintain external loading, and at the same time, suppress phonon reflection using the method that we have presented in the previous sections.

The general idea is the following: we express the quantities specified in the boundary conditions, such as the strain, the stress, and the velocity, at the atomic scale. We subtract off the mean values of these quantities and only control the remainder that represent the small scale components. Then we make use of the harmonic approximation to find the Fourier representation of these quantities, i.e. the remainder, which should be related to the Fourier coefficients of the displacement, $\hat{\mathbf{u}}(k)$. This allows us to compute the energy flux (3.40) using the Fourier coefficients of these quantities. After that we follow the same procedure as before to obtain the boundary condition. Next we discuss these cases in more detail.

4.3.1 Displacement boundary condition

In this case, the mean displacement $\bar{\mathbf{u}}(\mathbf{r}, t)$ is given. Assuming that $\bar{\mathbf{u}}$ has small variation at the atomic scale, we can decompose the displacement of the boundary atoms into the mean part and the small scale component,

$$\mathbf{u}_i = \bar{\mathbf{u}}(\mathbf{r}_i, t) + \mathbf{u}_i'. \tag{4.3}$$

Using $\sum_j D_j = 0$, one finds that $\mathbf{u}_i'$ also satisfies the linearized Newton's equation (3.20). Now we apply the boundary conditions (3.31) on $\mathbf{u}_i'$. After obtaining $\mathbf{u}_i'$ for the boundary atoms, we use (4.3) to update the displacement $\mathbf{u}_i$.

4.3.2 Imposing an applied deformation gradient

We next discuss how to maintain a specified deformation at the boundary. More precisely, we would like to impose,

$$\boldsymbol{\epsilon} = \frac{\partial \mathbf{u}}{\partial \mathbf{n}}, \tag{4.4}$$

at the boundary with normal vector $\mathbf{n}$.

As suggested by (4.4) we choose the new variables

$$\boldsymbol{\epsilon}_j = (\mathbf{u}_j - \mathbf{u}_{j_n})/d_n - \bar{\boldsymbol{\epsilon}}, \tag{4.5}$$

where j_n designates the next atom in the normal direction, d_n is the distance of this atom from the jth atom, and $\bar{\boldsymbol{\epsilon}}$ is the deformation applied at the boundary. The Fourier coefficients of $\{\boldsymbol{\epsilon}_j\}$ is related to that of $\{\mathbf{u}_j\}$

$$\hat{\boldsymbol{\epsilon}}(\mathbf{k}) = \hat{\mathbf{u}}(\mathbf{k})(1 - e^{id_n \mathbf{k}\cdot\mathbf{n}}).$$

Hence one may express the energy flux in terms of $\hat{\boldsymbol{\epsilon}}(\mathbf{k})$.

Boundary conditions can now be formulated for $\boldsymbol{\epsilon}_j$: we will seek boundary conditions in the form,

$$\boldsymbol{\epsilon}_0 = \sum_j \int_0^{t_0} \boldsymbol{\alpha}_j(\tau)\boldsymbol{\epsilon}_j(t-\tau)d\tau.$$

After the local deformation $\boldsymbol{\epsilon}_j$ is obtained from the boundary condition, we obtain the displacement using

$$\mathbf{u}_j = \big(\boldsymbol{\epsilon}_j + \bar{\boldsymbol{\epsilon}}\big)d_n + \mathbf{u}_{j_n},$$

which will be used for the force calculation.

4.3.3 Imposing an applied stress

Suppose that the material is subject to dead loading, namely we specify the traction:

$$\mathbf{t} = \mathbf{P}\mathbf{n},$$

where $\mathbf{P}$ is the first Piola-Kirchhoff stress. At the atomic scale, the traction is equal to the net interatomic force (per unit area) across the boundary,

$$\mathbf{t}_i = \frac{1}{\Omega_n} \sum_{\mathbf{r}_j \cdot \mathbf{n} < 0} \mathbf{f}_{ij}.$$

Here Ω_n denotes the average area per atom on the plane of the boundary. With harmonic approximation, this will be reduced to,

$$\mathbf{t}_i = \frac{1}{\Omega_n} \sum_{\mathbf{r}_j \cdot \mathbf{n} < 0} D_{i-j} \mathbf{u}_j,$$

which has Fourier coefficient

$$\hat{\mathbf{t}}(\mathbf{k}) = \frac{1}{\Omega_n} \sum_{l=-Ne}^{-1} \hat{D}_l e^{-ila_n}\, \hat{\mathbf{u}}(\mathbf{k}),$$

with $\hat{D}_l$ defined in (3.28).

Therefore the boundary condition can be reformulated for $\mathbf{t}_i$ in the same way as before. The $\mathbf{t}_i$ obtained from the boundary condition will be added to the force $\mathbf{f}_i$ to advance the system. It is not necessary to compute the displacement of the boundary atoms in this case.

4.4 Boundary conditions at the corners

We have discussed the boundary conditions for the case where the boundary coincide with a major symmetry plane. In practice, the boundary consists of a number of planes. Problems arise at the corners where two different planes intersect: the stencils will overlap or extends to the outside of the system. In this case, we create an artificial boundary for the corner atoms, and use different stencils. Similar techniques have been used in [15].

We illustrate this idea using the triangular lattice as an example. In Fig. 19 we plot the atoms of the triangular lattice near the lower left corner. For the boundary atoms away from the corner, the stencil is within the system and we can apply boundary conditions discussed above. The atoms at the corner are separated from the rest of the system by a plane with normal direction of 30 degrees. Now one can view this plane as a boundary and choose a stencil which stays in the system.

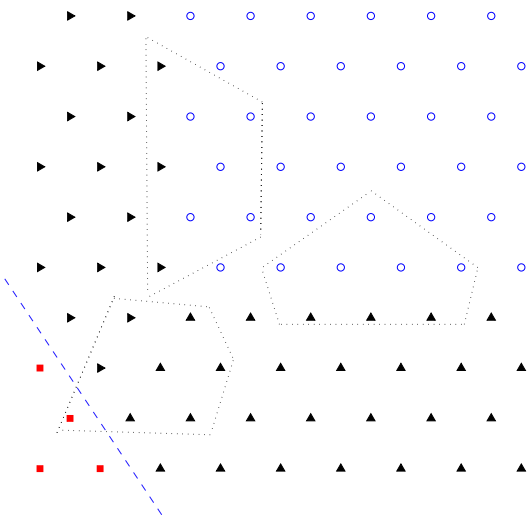

Figure 19: Classify the atoms at the corner: circles: the atoms in the interior of the system; triangles: the atoms at the horizonal and the vertical boundary; squares: atoms at the lower left corner. Different stencils $|J| = 8$ are used for different kind of atoms. In each case, one boundary atom is chosen and the atoms involved in its boundary condition are surrounded by dotted lines. The dashed line is the 'boundary' for the atoms at the corner.

5 An applications: fracture simulations

In this section, we apply the boundary conditions to molecular dynamic simulation of crack propagation in a 2D Lennard-Jones crystal. The difficulty due to phonon reflection for simulating crack propagation in such a system has been very well illustrated in the work of Holian and his co-workers [17, 19]. Our simulations are conducted with a similar setup: we start with a system consisting of about 20,000 atoms. A crack is formed at the left boundary by removing atoms within an elliptical notch. A uniform uniaxial strain rate is imposed along the y direction to open up the crack. The strain rate is $\epsilon_0 = 0.0004$ initially and is gradually reduced,

$$\dot{\epsilon} = \frac{\dot{\epsilon}_0}{1 + \dot{\epsilon}_0 t}. \tag{5.1}$$

The displacement at the boundary $\bar{\mathbf{u}}$ will be computed from (5.1) and imposed at the boundaries.

To be readily compared to the results from [17, 19], we use the same techniques for the boundaries on the top and bottom: we first subtract $\bar{\mathbf{u}}$ from the actual displacement, and then apply periodic boundary condition on the remaining displacement. This is an effective technique for maintaining constant uniaxial strain.

In the first experiment fixed boundary condition is applied on the right, i.e. $\mathbf{u}_j = \bar{\mathbf{u}}(\mathbf{r}_j, t)$, while in the second experiment, we apply VBC with $|J| = 8$ and $M = 10$. The results are shown at the instant $t = 51.0$ in Fig. 20 and Fig. 21 respectively. The units are the same as those

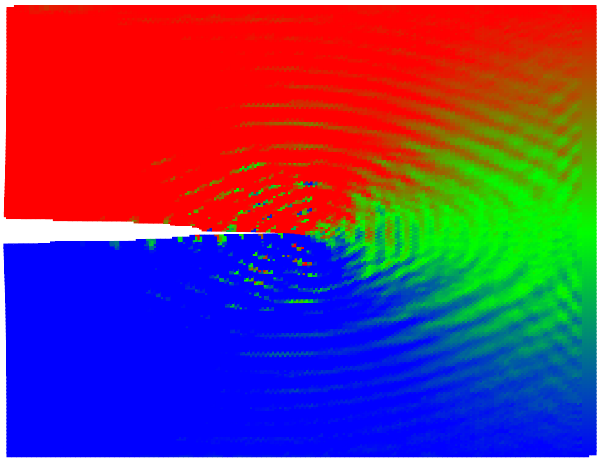

Figure 20: Simulation of crack propagation using fixed boundary condition: the color scheme was selected according to the vertical component of the velocity.

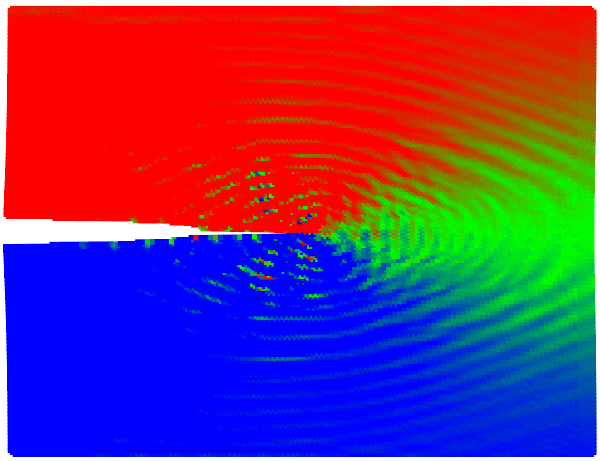

Figure 21: Simulation of crack propagation using variational boundary condition (3.35) with $\{J = 8, M = 20\}$. The color scheme was selected according to the vertical component of the velocity.

in section 3.4.2. Both experiments show the propagation of a brittle crack. As the crack opens up, a large amount of phonons are being emitted. These phonons will propagate to the right and soon reach the boundary. Fig. 20 for the results with the fixed boundary condition clearly shows phonon reflection at the right boundary. In contrast, one sees from Fig. 21 that VBC is quite effective in suppressing the reflection.

In [17, 19] extensive numerical simulations with different size and boundary conditions have been conducted. It was found that the reflection of phonons can completely change the crack tip behavior. Therefore boundary conditions become a crucial component in these kind of

numerical studies. Currently our variational boundary conditions are being implemented to study the dynamics of brittle cracks.

6 Comparison with adding border atoms

Another alternative for preventing wave reflection is to append an additional border region to the computational domain. The principal idea is to create an absorbing layer of finite thickness to annihilate outgoing waves. A common technique is to add damping in the layer with a damping coefficient d, which is often chosen to be zero at the boundary between the original system and the border region, and positive away from the boundary to damp out the waves. Choosing appropriate damping coefficient is the key to the effectiveness of these methods. For continuum wave equation, the border region and the computational domain can be matched perfectly, i.e. with no reflection [5]. This is known as perfect matched layers method (PML), which has been very successful.

The perfect matching cannot be achieved, however, for the discrete case as pointed out in [8]. But similar ideas have been explored by various people for MD simulations [19, 20, 31]. For example in [31], the authors considered a one dimensional MD model and adopted the PML method for elastodynamics [8]. In particular they proposed the following equations for the border region,

$$m\ddot{u}_j = -\frac{\partial V}{\partial u_j} - md(r_j)^2 u_j - 2md(r_j)\dot{u}_j. \tag{6.1}$$

In principle, one can also use the variational formalism proposed in this paper to find the optimal damping coefficients. In practice, however, it is not known how to compute the reflection matrix in this case.

Here we will make a quantitative comparison between the damping method and the VBC by computing the reflection coefficients for the two methods. As an example, the 1D chain model (3.10) is considered. For the variational boundary condition, the reflection coefficient is obtained from (3.48), while for the damping method, it is computed numerically. Specifically, we conduct a series of simulations, and in each simulation, we start with a wave packet,

$$u_j(0) = \int_{-\pi}^{\pi} A(k)e^{ik(j-j_0)}dk, \quad v_j(0) = -i\int_{-\pi}^{\pi} A(k)\omega(k)e^{ik(j-j_0)}dk. \tag{6.2}$$

Initially the center of the wave packet is located at $j = j_0 > 0$. The function $A(k) = e^{-(k-k_0)^2/2\epsilon}/\sqrt{2\pi\epsilon}$ has the shape of a Gaussian. By choosing small ϵ, one can focus the wavenumber in the wave packet around k_0. Numerous values of $k_0 \in (-\pi, 0)$ are chosen. Since $\omega'(k_0) < 0$ the wave packet will propagate to the left until it arrives at the boundary. Due to the applied boundary condition, a reflected wave packet with the opposite group velocity will emerge from the boundary and reenter the domain. We will define the reflection coefficient $R(k_0)$ to be the ratio between the maximal amplitude of the reflected and the incident wave. The damping coefficient is chosen according to the one used in [8, 31],

$$d(x) = -\frac{3V}{2}\log(R)\frac{x^2}{\delta^3}. \tag{6.3}$$

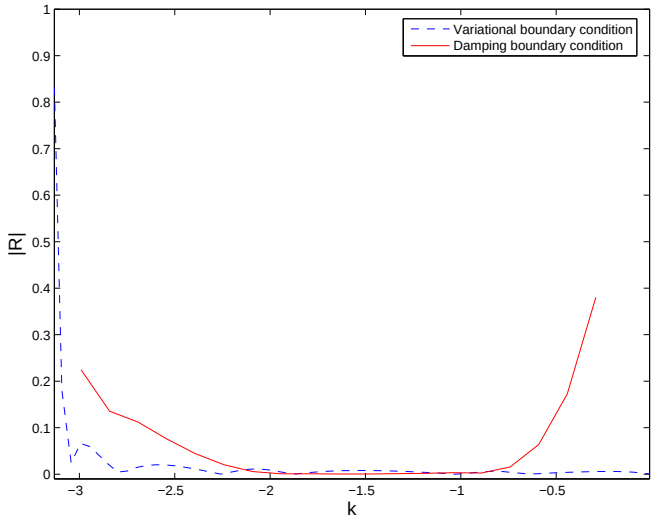

Figure 22: The reflection coefficients resulting from a damping boundary condition and a variational boundary condition for the one dimensional chain model (3.10).

Here δ is the width of the border region. $V = 1$ is the elastic wave speed and $R < 1$ is a free parameter.

In Fig. 22, the reflection coefficients corresponding to the two methods are plotted. In the case shown there are ten atoms in the damping region for the damping boundary condition, $\delta = 10$, and the variational boundary condition involves ten atoms and two time steps, $|J| = 10$ and $M = 2$. One can see that the variational boundary condition suppresses phonon reflection for most wavenumbers, while the damping boundary condition leads to considerable reflection for $k_0 < -2.5$ and $k_0 > -0.5$. The performance can be improved by increasing the thickness of the layer. However in a 3D simulation, this may dramatically increase the size of the system as well as the computational cost.

7 Conclusion

To put things in perspective, let us go back to the analogy with the wave equations. There are two main approaches in suppressing wave reflection at the boundary. One is the absorbing boundary condition (ABC) [14, 15]. The other is to use perfectly matched layers (PML) [5], which is analogous to the popular MD technique of padding with border regions in order to damp out the phonons. In general, PML is more accurate and has become more popular. But for discrete cases, perfect matching can not be achieved as indicated in [8] and it is not clear how the damping coefficients can be chosen to optimize the performance of the method. Furthermore, if a domain decomposition approach is used where wave equation is solved in conjunction with continuum equations in the neighboring domain, ABC is still a more convenient choice.

The variational boundary condition (VBC) presented here represents a compromise. In principle, it can be used in either an ABC or PML setting, except that the coefficients are numerically computed using a variational formalism that minimizes phonon reflection. This is necessary for MD since in that case the waves are too complicated and as a result, not many analytical formulas are available. However, even for the continuous problem, VBC might be a viable alternative to the existing techniques of ABC and PML.

Another important issue is temperature. Here we focused on low temperature systems where the main objective is to absorb the phonons coming to the boundary. At finite temperature, the system absorbs energy from phonons provided by the environment. This issue remains open.

At a technical level, the technicalities involved in finding the VBC are very similar to that of phonon analysis. Even though for realistic systems, they are far from being trivial, they are not worse than finding the exact boundary conditions as suggested in [1, 2, 22, 32], or computing them numerically as suggested in [6]. The main input parameters are the force constants. Aside from the phonon analysis step, there is the step of minimization of the total reflected energy flux. Both steps can be standardized. Once the VBCs are found, the are much more efficient than the exact boundary conditions.

References

[1] S. A. Adelman and J. D. Doll, Generalized Langevin equation approach for atom/solid-surface scattering: Collinear atom/harmonic chain model, J. Chem. Phys., 61 (1974), 4242–4245.

[2] S. A. Adelman and J. D. Doll, Generalized Langevin equation approach for atom/solid-surface scattering: General formulation for classical scattering off harmonic solids, J. Chem. Phys., 64 (1976), 2375–2388.

[3] A. Arnold, M. Ehrhardt and I. Sofronov, Approximation, stability and fast calculation of non-local boundary conditions for the Schrödinger equation, Comm. Math. Sci., 1(3) (2003), 501–556.

[4] N. W. Ashcroft and N. D. Mermin, Solid State Physics, Holt, Rinehart and Winston, New York, 1976.

[5] J. P. Berenger, Three-dimensional perfectly matched layer for the absorption of electromagnetic waves, J. Comp. Phys., 127 (1996), 363–379.

[6] W. Cai, M. de Koning, V. V. Bulatov and S. Yip, Minimizing boundary reflections in coupled-domain simulations, Phys. Rev. Lett., 85 (2000), 3213–3216.

[7] K. Cheung and S. Yip, A molecular-dynamics simulation of crack-tip extension: the brttle-to-ductile transition, Model. Simul. Mater. Sci. Engrg., 2 (1994), 865–892.

[8] F. Collino and C. Tsogka, Application of the perfectly matched absorbing layer model to the linear elastodynamic problem in anisotropic heterogeneous media, Geophysics, 66 (2001), 294–307.

[9] M. S. Daw and M. I. Baskes, Embedded-atom method: derivation and application to impurities, surfaces, and other defects in metals, Phys. Rev. B, 29 (1984), 6443–6453.

[10] W. E and B. Engquist, The heterogeneous multi-scale methods, Comm. Math. Sci., 1 (2003), 87–132.

[11] W. E and Z. Huang, Matching conditions in atomistic-continuum modeling of material, Phys. Rev. Lett., 87 (2001), 135501.

[12] W. E and Z. Huang, A dynamic atomistic-continuum method for the simulation of crystalline material, J. Comp. Phys., 182 (2002), 234–261.

[13] M. Ehrhardt and A. Arnold, Discrete transparent boundary conditions for the Schrödinger equation, Revista di Matematica della Universita di Parma 6/4, (2001), 57–108.

[14] B. Engquist and A. Majda, Absorbing boundary conditions for the numerical simulation of waves, Math. Comput, 31 (1977), 629–651.
[15] B. Engquist and A. Majda, Radiation boundary conditions for acoustic and elastic wave calculations, Comm. Pure Appl. Math., 32(3) (1979), 314–358.
[16] S. Froyen, Brillouin-zone integration by Fourier quadrature: special points for superlattice and supercell calculations, Phys. Rev. B, 39 (1989), 3168–3172.
[17] P. Gumbsch, S. J. Zhou and B. L. Holian, Molecular dynamics investigation of dynamic crack stability, Phys. Rev. B, 55 (1997), 3445–3455.
[18] L. Halpern, Absorbing boundary conditions for the discretization schemes of the one-dimensional wave equation, Math. Comput, 158 (1982), 415–429.
[19] B. L. Holian and R. Ravelo, Fracture simulation using large-scale molecular dynamics, Phys. Rev. B., 51 (1995), 11275–11288.
[20] D. Holland and M. Marder, Ideal brittle fracture of silicon studied with molecular dynamics, Phys. Rev. Lett., 80 (1998), 746–749.
[21] J. H. Irving and J. G. Kirkwood, The statistical mechanical theory of transport processes IV, J. Chem. Phys. 18, (1950) 817–829.
[22] E. G. Karpov, G. J. Wagnery and W. K. Liu, A Green's function approach to deriving non-reflecting boundary conditions in molecular dynamics simulations, Int. J. Numer. Methods Engrg., 62(9) (2005), 1250–1262.
[23] G. Kresse, J. Furthmüller and J. Hafner, Ab initio force constant approach to phonon dispersion relations of diamond and graphite, Europhys. Lett., 32(9) (1995), 729–734.
[24] X. Li and W. E, Multiscale modeling for dynamics of solids at finite temperature, J. Mech. Phys. Solids, 56 (2005), 1650–1685.
[25] H. J. Monkhorst and J. D. Pack, Special point in Brillouin-zone integrations, Phys. Rev. B, 13 (1976), 5188–5192.
[26] M. Musgrave, Crystal Acoustics, Holden-Day, San Francisco, 1970.
[27] H. S. Park, E. G. Karpov, W. K. Liu and P. A. Klein, The bridging scale for two-dimensional atomistic/continuum coupling, Philos. Mag., 85 (2005), 79–113.
[28] V. Shastry and D. Farkas, Molecular statics simulation of crack propagation in alpha-Fe using EAM potentials, in: F. A. Ponce, R. D. Dupuis, S. Nakamura and J. A. Edmond (Eds.), Materials Research Society Symposium Proceedings, vol. 395, MRS, Pittsburgh, 1996, pp. 75–80.
[29] P. Taborek and D. Goodstein, Phonon reflection at a sapphire-vacuum interface, J. Phys. C: Solid State Phys., 12 (1979), 4737–4751.
[30] J. Tersoff, New empirical model for the structural properties of silicon, Phys. Rev. Lett., 56 (1986), 632–635.
[31] A. C. To and S. Li, Perfectly matched multiscale simulations, Phys. Rev. B, 72 (2005), 035414.
[32] G. J. Wagner, E. G. Karpov and W. K. Liu, Molecular dynamics boundary conditions for regular crystal lattice, Comput. Method Appl. Mech. Engrg., 193 (2004), 1579–1601.
[33] C. Zhu, R. H. Byrd and J. Nocedal, L-BFGS-B: Algorithm 778: L-BFGS-B, FORTRAN routines for large scale bound constrained optimization, ACM T. Math. Software, 23(4) (1997), 550–560.